

ACTIVE GALACTIC NUCLEI WITH ULTRA-FAST OUTFLOWS MONITORING PROJECT: THE BROAD-LINE REGION OF MRK 79 AS A DISK WIND

KAI-XING LU^{1,2,11}, JIN-MING BAI^{1,2,11}, ZHI-XIANG ZHANG³, PU DU⁴, CHEN HU⁴, MINJIN KIM^{5,6}, JIAN-MIN WANG^{4,11}, LUIS C. HO^{7,8}, YAN-RONG LI⁴, WEI-HAO BIAN⁹, YE-FEI YUAN¹⁰, MING XIAO⁴, HAI-CHENG FENG^{1,2}, JIAN-GUO WANG^{1,2}, LIANG XU^{1,2}, XU DING^{1,2}, XIAO-GUANG YU^{1,2}, YU-XIN XIN^{1,2}, KAI YE^{1,2}, CHUAN-JUN WANG^{1,2}, BAO-LI LUN^{1,2}, JU-JIA ZHANG^{1,2}, XI-LIANG ZHANG^{1,2}, KAI-FAN JI¹, YU-FENG FAN^{1,2}, LIANG CHANG^{1,2}

¹Yunnan Observatories, Chinese Academy of Sciences, Kunming 650011, People's Republic of China

²Key Laboratory for the Structure and Evolution of Celestial Objects, Chinese Academy of Sciences, Kunming 650011, People's Republic of China

³Department of Astronomy, Xiamen University, Xiamen, Fujian 361005, People's Republic of China

⁴Key Laboratory for Particle Astrophysics, Institute of High Energy Physics, Chinese Academy of Sciences, 19B Yuquan Road, Beijing 100049, People's Republic of China

⁵Department of Astronomy and Atmospheric Sciences, Kyungpook National University, Daegu 702-701, Republic of Korea

⁶Korea Astronomy and Space Science Institute, Daejeon 305-348, Republic of Korea

⁷Kavli Institute for Astronomy and Astrophysics, Peking University, Beijing 100871, People's Republic of China

⁸Department of Astronomy, School of Physics, Peking University, Beijing 100871, People's Republic of China

⁹Physics Department, Nanjing Normal University, Nanjing 210097, People's Republic of China

¹⁰Department of Astronomy, University of Science and Technology of China, Hefei 230026, People's Republic of China

¹¹Corresponding authors: lukx@ynao.ac.cn, baijinming@ynao.ac.cn, wangjm@ihep.ac.cn

ABSTRACT

We developed a spectroscopic monitoring project to investigate the kinematics of the broad-line region (BLR) in active galactic nuclei (AGN) with ultra-fast outflows (UFOs). Mrk 79 is a radio-quiet AGN with UFOs and warm absorbers, had been monitored by three reverberation mapping (RM) campaigns, but its BLR kinematics is not understood yet. In this paper, we report the results from a new RM-campaign of Mrk 79, which was undertaken by Lijiang 2.4-m telescope. Mrk 79 is seeming to come out the faint state, the mean flux approximates a magnitude fainter than historical record. We successfully measured the lags of the broad emission lines including H β λ 4861, H γ λ 4340, He II λ 4686 and He I λ 5876 with respect to the varying AGN continuum. Based on the broad H β λ 4861 line, we measured black hole (BH) mass of $M_{\bullet} = 5.13^{+1.57}_{-1.55} \times 10^7 M_{\odot}$, estimated accretion rates of $\dot{M}_{\bullet} = (0.05 \pm 0.02) L_{\text{Edd}} c^{-2}$, indicating that Mrk 79 is a sub-Eddington accretor. We found that Mrk 79 deviates from the canonical Radius–Luminosity relationship. The marginal blueshift of the broad He II λ 4686 line detected from rms spectrum indicates outflow of high-ionization gas. The velocity-resolved lag profiles of the broad H γ λ 4340, H β λ 4861, and He I λ 5876 lines show similar signatures that the largest lag occurs in the red wing of the lines then the lag decreases to both sides. These signatures should suggest that the BLR of Keplerian motion probably exists the outflow gas motion. All findings including UFOs, warm absorbers, and the kinematics of high- and low-ionization BLR, may provide an indirect evidence that the BLR of Mrk 79 probably originates from disk wind.

Keywords: galaxies: active – galaxies: nuclei – galaxies: individual (Mrk 79)

1. INTRODUCTION

In the past thirty years, reverberation mapping (RM; Bahcall et al. 1972; Blandford & McKee 1982) has been extensively adopted to investigate the kinematics of the broad-line region (BLR) and measure the mass of accreting supermassive black hole (BH) in active galactic nuclei (AGN). BH masses of ~ 100 AGNs have been measured by different RM campaigns (e.g., Peterson et al. 1993b, 1998; Kaspi et al. 2000; Peterson et al. 2004; Denney et al. 2009b, 2010; Bentz et al. 2007, 2009b, 2010, 2013; Barth et al. 2011a,b; Peterson 2014; Du et al. 2015; Grier et al. 2017; Du et al. 2018; De Rosa et al. 2018). Canonical Radius–Luminosity relationship is constructed from these RM campaigns

(Peterson et al. 1993b; Wandel et al. 1999; Kaspi et al. 2000; Bentz et al. 2013), which provides an indirect way to estimate BH mass from single spectrum. However, as the number of sample increases, this relationship becomes more scatter (~ 0.3 dex; Bentz et al. 2013; Grier et al. 2017; Du et al. 2018). It is possible to find the physics of this scatter studying the long-term variation of the BLR by repeated RM-campaign (Peterson et al. 2002; Lu et al. 2016). The kinematic structures of the BLR for ~ 20 AGNs have been probed using velocity-resolved RM (e.g., Denney et al. 2009a, 2010; Bentz et al. 2009b, 2010; Barth et al. 2011a,b; Grier et al. 2013; Du et al. 2016; Lu et al. 2016; Pei et al. 2017; De Rosa et al. 2018; Zhang et al. 2019). They usu-

ally include virialized disk, inflow, and outflow (Bentz et al. 2009b; Grier et al. 2013), but physical origins of inflow and outflow remain unclear.

Mrk 79 is a nearby and radio-quiet (RQ) AGN ($z = 0.022189$ from NED), which has been monitored by three RM-campaign (Peterson et al. 1998). These campaigns successfully detected time delays of the broad $H\beta$ line with respect to the continuum variation, but the BLR’s kinematics of Mrk 79 is not understood yet. Therefore, Mrk 79 deserves to be monitored again to investigate the kinematics of the BLR, and to construct the Radius–Luminosity relationship of Mrk 79 (like Radius–Luminosity relationship of NGC 5548, see Peterson et al. 2002; Lu et al. 2016; Pei et al. 2017; Kriss et al. 2019).

Secondly, based on X-ray spectrum between 7 and 10 keV, ultra-fast outflows (UFOs, i.e., highly ionized absorbers) have been detected in Mrk 79 through Fe XXV and Fe XXVI K-shell absorption lines with blueshifted velocity $V_{\text{UFOs,out}} = (0.092 \pm 0.004)c$ (c is the speed of light, see Tombesi et al. 2010, 2011). Warm absorbers also detected in soft X-ray spectrum, but current energy resolution of X-ray spectrum is hard to constrain its nature (Gallo et al. 2011; Tombesi et al. 2013). UFOs and warm absorbers are probably associated with accretion disk wind in Mrk 79 because it is a RQ AGN (no jets; Tombesi et al. 2011). What is the connection between the BLR and accretion disk wind?

On the one hand, multiphase disk wind including hard X-ray absorbers (UFOs), soft X-ray absorbers (warm absorbers), and UV absorbers were confirmed in term of the blueshift of X-ray and ultraviolet (UV) broad absorption lines (e.g., Murray & Chiang 1997; Leighly & Moore 2004; O’Brien et al. 2005; Tombesi et al. 2010, 2013; Hamann et al. 2018; Longinotti et al. 2019; Giustini & Proga 2019), in which these absorbers jointly or partially exist in AGNs (O’Brien et al. 2005; Tombesi et al. 2013). Therefore a disk wind model characterised by multiphase stratified structure was developed to explain these phenomenons (e.g., see Figure 5 of Tombesi et al. 2013, Figure 6 of Mas-Ribas 2019). In addition, outflows of the BLR are also found from UV and optical spectra. For example, (1) Richards et al. (2011) found that the blueshift of broad C IV emission line are nearly ubiquitous, with a mean velocity of $\sim 810 \text{ km s}^{-1}$ for RQ AGNs; (2) in RM study of spectroscopic monitoring, Hu et al. (2015) found that a blueshifted broad He II $\lambda 4686$ line is need to reasonably decompose optical spectrum; (3) based on the rest frame defined by [O III] $\lambda 5007$ line, Ge et al. (2019) found the blueshift of the broad C IV emission line has a medium-strong positive correlation with the optical luminosity and the Eddington ratio. Murray et al. (1995) developed a model for line-driven wind from accretion disk, which suggested that the absorbing gas cannot lie within the broad-line emitting region but can be co-spatial with it or outside of it, and predicted that the high-ionization emission lines should be blueshifted relative to the low-ionization emission lines. Interestingly, the blueshift of absorbers and emitters jointly exist in a few AGNs (e.g., PDS 456). O’Brien et al. (2005) attributed this phenomenon to a decelerating, cooling outflow, which may be driven by

radiation and/or magnetic field, and suggested that the X-ray outflow could be the source of some of the BLR gas. In this case, the geometric and kinematic structures of the BLR could be modified by decelerating, cooling outflow.

On the other hand, The signature of the outflowing BLR was just observed doubtlessly by velocity-resolved RM in Mrk 142 and NGC 3227 (Du et al. 2016; Denney et al. 2009a, 2010). It’s worth noting that these both AGNs have different properties. Mrk 142 has very high accretion rates, radiation pressure acting on the ionized gas may drive outflow of the BLR (Du et al. 2015). However, NGC 3227 is a low-accretion AGN (Denney et al. 2010; Du et al. 2015), but has detected outflows of hard X-ray and soft X-ray absorbers with velocity of $\sim 2060 \text{ km s}^{-1}$ and $\sim 420 \text{ km s}^{-1}$ (i.e., UFOs and warm absorbers) from X-ray spectrum (Markowitz et al. 2009). What drives outflow of the BLR for AGNs in the low accretion rate?

Motivated by above questions, we will focus on investigating the BLR kinematics of AGNs with UFOs and explore potential connection between the BLR and UFOs (or accretion disk wind). Therefore we developed an AGNs with UFOs monitoring project, this paper presents the results from the spectroscopic monitoring of Mrk 79. The paper is organized as follows. In Section 2, we describe the observation and the data reduction in detail. Data analysis and results including spectral measurement, time series analysis, the construction of velocity-resolved lag profiles and estimate black hole mass and so on are present in Section 3. Section 4 is discussion and summary is given in Section 5. We use a cosmology with $H_0 = 67 \text{ km s}^{-1} \text{ Mpc}^{-1}$, $\Omega_\Lambda = 0.68$, and $\Omega_M = 0.32$ (Planck Collaboration et al. 2014),

2. OBSERVATION AND DATA REDUCTION

2.1. Spectroscopic and Photometric Observation

The spectroscopic and photometric observation of Mrk 79 were taken using Yunnan Faint Object Spectrograph and Camera (YFOSC) mounted on the Lijiang 2.4-m telescope (LJT), which is located at Lijiang observatory and is administered by Yunnan Observatories of Chinese Academy of Sciences (Fan et al. 2015; Wang et al. 2019). YFOSC is equipped with a back-illuminated 2048×2048 pixel CCD, with pixel size $13.5 \mu\text{m}$, pixel scale $0.283''$ per pixel, and field-of-view $10' \times 10'$. It is a versatile instrument for low-resolution spectroscopy and photometry (see Du et al. 2014; Lu et al. 2016).

The spectral monitoring of Mrk 79 started on 2017 November 1, and terminated on 2018 March 13. During the spectroscopic observation, we simultaneously observed a nearby comparison star along the slit as a reference standard, which can provide high-precision flux calibration (see Hu et al. 2015; Lu et al. 2016; Du et al. 2018). This observation method was described in detail by Maoz et al. (1990) and Kaspi et al. (2000), and was recently adopted by (Du et al. 2014; Lu et al. 2016; Du et al. 2018). In the light of the average seeing $\sim 1.3''$ of observational station, we fixed the projected slit width $2.5''$. We used Grism 14, which provides a resolution 92 \AA mm^{-1} ($1.8 \text{ \AA pixel}^{-1}$) and covers the wavelength range $3600\text{--}7460 \text{ \AA}$. Standard neon and helium

lamps were used for wavelength calibration. In total, we obtained 72 spectroscopic observations, spanning a observation period of 132 days. The median and mean cadences are 1.0 and 1.8 days, respectively. All spectra were observed with a median air mass of 1.15, which means that atmospheric differential refraction has a negligible impact on our analysis (Filippenko 1982).

It should be noted that the standard spectral calibration method assumes that the [O III] $\lambda 5007$ flux is constant and use it as an internal flux calibrator (e.g., Fausnaugh 2017). To integrally put extended [O III] $\lambda 5007$ emission region into the slit in spectroscopy, many previous RM campaigns adopted a broad slit ($\sim 5''$; see Table 12 of Bentz et al. 2013) at the cost of losing the spectral resolution. In this case, standard spectral calibration method using the [O III] $\lambda 5007$ as calibrator provides precise internal flux calibration of spectra (see Fausnaugh 2017). Actually, a relatively narrow slit contributes to increasing the spectral resolution, and high spectral resolution is conducive to the following velocity-resolved time series analysis (Section 3.8). Therefore, we adopted a relatively narrow slit ($2.5''$) in spectroscopy. For a small spectrograph slit, using the [O III] $\lambda 5007$ as an internal flux calibrator is not an optimal choice, because the [O III] $\lambda 5007$ emission region of many AGNs (e.g., Schmitt et al. 2003a,b, and Peterson et al. 1995 for NGC 4151) along with the host galaxy are (slightly and very) extended sources (see Appendix A), varying observing conditions may cause the apparent variation in flux of extended sources (details refer to Appendix A). While, in this case, a stable comparison star observed along with the object simultaneously in a narrow slit can provide precise flux calibration of spectra (see Section 3.4 and Appendix A, Hu et al. 2015 as well).

The photometric images with the field of $10'' \times 10''$ were obtained using a Johnson V filter. Totally, we obtained 62 photometric observations. Typically, two exposures of 90 s were taken for each individual observation.

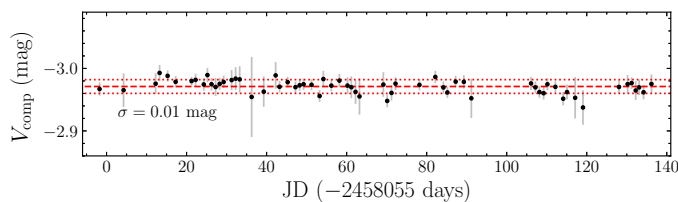


Figure 1. Light curves of the comparison star for the present campaign. The scatter of the light curves is 0.01 mag.

2.2. Data reduction

The photometric images were reduced following standard IRAF procedures using IRAF (v2.16) package. The magnitude of the object (Mrk 79) and the comparison star were measured through a circular aperture with radius of $5.7''$, and differential magnitudes were obtained relative to 4 selected stars within the field of view. Figure 1 shows the light curve of comparison star. The accurate of the photometry is 1%, which demonstrates that the comparison star is stable enough to be used for flux calibration of the spectra. The photometric

data of Mrk 79 will be used to check the spectral calibration in Section 3.4.

The two-dimensional spectroscopic data were reduced using the standard IRAF (v2.16) package. This process included bias subtraction, flat-field correction, wavelength calibration and spectrum extraction. All spectra were extracted using a uniform aperture of 20 pixels ($5.7''$), and background was determined from two adjacent regions ($+7.4'' \sim +14''$ and $-7.4'' \sim -14''$) on both sides of the aperture region. Actually, a relatively small extraction aperture contributes to reducing the poisson noise of sky background and increasing the signal-to-noise ratio (S/N) of spectrum. High S/N ratio is conducive to the following multi-component decomposition of spectrum (Section 3.2). Spectral flux of the target were calibrated by the comparison stars in two steps. (1) We produced the fiducial spectrum of the comparison star using data from nights with photometric conditions. (2) For each object/comparison star pair, we obtained a wavelength-dependent sensitivity function comparing the star's spectrum to the fiducial spectrum. Then this sensitivity function was applied to calibrate the observed spectrum of the target (also see Appendix A; Du et al. 2014; Lu et al. 2016).

2.3. Data processing

The flux-calibration spectra were corrected for Galactic extinction using the extinction map of Schlegel et al. (1998) at first. The variations of seeing and mis-centering usually cause slight wavelength shift and broadening of emission lines (Du et al. 2018; Lu et al. 2016). We corrected wavelength shift using [O III] $\lambda 5007$ line as wavelength reference, and corrected broadening of emission lines convoluting [O III] $\lambda 5007$ line into its maximum width determined from 72 spectra. Then spectra were transformed into the rest frame using the redshift ($z = 0.022189$). These processed spectra are adopted in the next analysis.

3. DATA ANALYSIS AND RESULTS

3.1. Mean and RMS Spectra

The definition of mean spectrum is (Peterson et al. 2004)

$$F_{\lambda} = \frac{1}{N} \sum_{i=1}^N F_i(\lambda) \quad (1)$$

and rms spectrum is

$$S_{\lambda} = \left\{ \frac{1}{N} \sum_{i=1}^N [F_i(\lambda) - \overline{F}(\lambda)]^2 \right\}^{1/2}, \quad (2)$$

where $F_i(\lambda)$ is the i th spectrum and N is the total number of spectra obtained during the monitoring period. Using Equations (1,2), we calculated the mean and rms spectrum of Mrk 79 from the processed spectra and showed them in Figure 2 (in blue). Zoom-in of mean spectrum was inserted in Figure 2a, which presents significant corona lines (such as [Fe VII] $\lambda\lambda 5158, 5178$, [Fe VII] $\lambda 5721$, [Fe VII] $\lambda 6086$ and [Ca V] $\lambda 5310$), narrow lines (e.g., He I $\lambda 4471$, He I $\lambda 5876$), and weak absorption-line features (e.g., see the red wing of He I $\lambda 5876$ narrow line). [O III] emission lines should

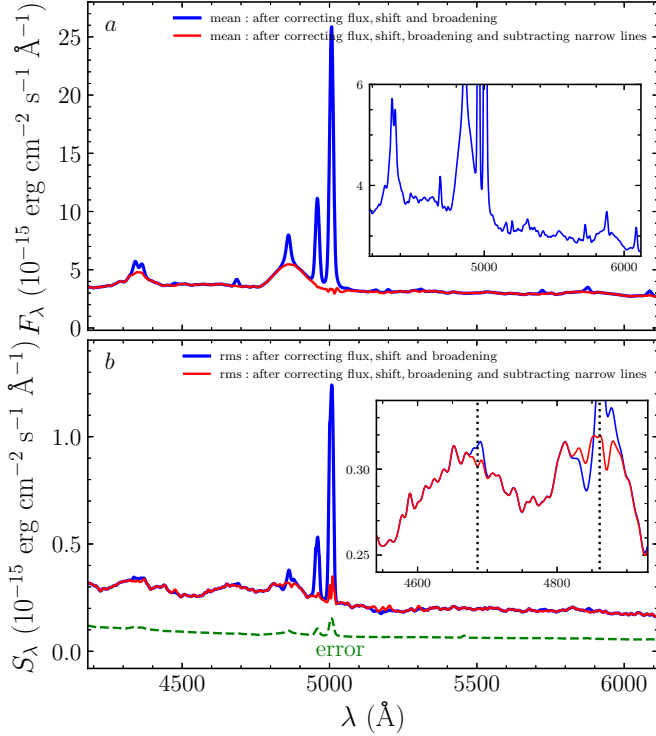


Figure 2. Panels show the mean (*a*) and rms (*b*) spectrum of Mrk79 in the rest frame, respectively. Blue lines are the original mean and rms spectrum calculated from processed spectra (see Section 2.3). Red lines are the revised mean and rms spectrum constructed after subtracting narrow emission lines (including $H\gamma\lambda 4340$, $[O\text{III}]\lambda 4363$, $\text{He I}\lambda 4471$, $\text{He II}\lambda 4686$, $[\text{Fe VII}]\lambda\lambda 5158, 5178$, $[\text{N I}]\lambda 5200$, $[\text{Ca V}]\lambda 5310$, $[\text{Fe VII}]\lambda\lambda 5721$, $\text{He I}\lambda 5876$ and $[\text{Fe VII}]\lambda 6086$) from each nightly spectrum. We only show the fitting region ($4180\text{\AA}-6115\text{\AA}$ in the rest frame, see Section 3.2).

normally disappear in rms spectrum because the flux of $[\text{O III}]\lambda\lambda 4959, 5007$ emission lines dramatically remain in rms spectrum.

In practice, two scenarios will result in the $[\text{O III}]\lambda\lambda 4959, 5007$ remaining in the rms spectrum. (1) Residual $[\text{O III}]\lambda\lambda 4959, 5007$ is caused by wavelength shift and broadening of emission line. (2) As considered in Section 2.1 (the third paragraph), residual $[\text{O III}]\lambda\lambda 4959, 5007$ may be attributed to the apparent variation in flux of $[\text{O III}]\lambda\lambda 4959, 5007$ caused by varying observing conditions because the narrow-line region (NLR) of Mrk 79 is slightly extended (Schmitt et al. 2003a,b; Ho 2009, also see Appendix A). For the former, we have processed spectra of Mrk 79 strictly before calculating rms spectrum, therefore the residuals of $[\text{O III}]\lambda\lambda 4959, 5007$ in rms spectrum do not caused by the shift and broadening of emission line. If the latter case holds, apparent variation in flux of $[\text{O III}]\lambda\lambda 4959, 5007$ and host-galaxy should have similar behaviour (or be correlated) because NLR and the host galaxy are extended sources, we will examine this in Section 3.4.

Based on the mean and rms spectrum, we found that the broad $\text{He II}\lambda 4686$ is very weak (see blue trace of Figure 2a), but its flux shows significant variation (see blue trace of Figure 2b) during the monitoring period. To determine the width of the broad $\text{He II}\lambda 4686$ line from the rms spectrum, we run 200 Monte Carlo simulations similar to the method

adopted by Grier et al. (2012). We created 200 rms spectra from 200 randomly chosen subsets of the spectra, and obtained distributions of line width (FWHM) and positions of line core (C). The distributions give $\text{FWHM}_{\text{He II}\lambda 4686} = 9621 \pm 812 \text{ km s}^{-1}$ and $C_{\text{He II}\lambda 4686} = 4678.6 \pm 3.9 \text{\AA}$. The latter corresponds to a blueshift of the broad $\text{He II}\lambda 4686$ emission line with velocity of $\sim 450 \text{ km s}^{-1}$.

3.2. Spectral Fitting

To more accurately separate the broad emission features from each other, spectral fitting scheme (SFS) is widely used in the spectroscopic measurements of AGN (e.g., Hu et al. 2008; Wang et al. 2009; Dong et al. 2008, 2011; Stern & Laor 2012; Jin et al. 2012; Liu et al. 2018; Lu et al. 2019). Especially, in the study of reverberation mapping field, SFS has been proven to be necessary to measure the light curves when broad emission line blended highly with each other (Bian et al. 2010; Hu et al. 2015; Barth et al. 2013, 2015). Beyond that, by modelling and removing the contamination of strong host galaxy which varies from night to night due to seeing and guiding variations, SFS can improve the measurement quality of light curves of continuum and broad emission lines (Hu et al. 2015, 2016).

In order to decompose the spectra of Mrk 79 using SFS, we followed previous method described by Hu et al. (2015) with some changes described below. The fitting was performed in the rest wavelength range $4180 \text{\AA}-6115 \text{\AA}$, which has no effect of the second-order (secondary spectrum) in our analysis because it's contamination occurs longer than 6250\AA . The fitting components include: (1) a single power law ($f_\lambda \propto \lambda^\alpha$, α is the spectral index) for the AGN continuum. In practice, a single power-law is successfully used to fit AGN continuum over a broad region ($\sim 4150 \text{\AA}-6200 \text{\AA}$; Hu et al. 2015); (2) the starlight from the host galaxy modelled by the template with 11 Gyr age and metallicity $Z = 0.05$ from Bruzual & Charlot (2003); (3) Fe II multiplets modelled by Fe II template from Boroson & Green (1992) convolving with a Gaussian function; (4) four single Gaussians for the broad-emission lines including $H\beta\lambda 4861$, $H\gamma\lambda 4340$, $\text{He II}\lambda 4686$, and $\text{He I}\lambda 5876$, respectively; (5) three double Gaussians for the $[\text{O III}]\lambda\lambda 5007/\lambda 4959$ and $H\beta\lambda 4861$ narrow line; (6) a set of several single Gaussians with the same velocity width and shift for narrow emission lines including $H\gamma\lambda 4340$, $[\text{O III}]\lambda 4363$, $\text{He I}\lambda 4471$, $\text{He II}\lambda 4686$, $\text{He I}\lambda 5876$, $[\text{N I}]\lambda 5200$ and several coronal lines. Following Hu et al. (2015), we fitted the above models simultaneously to the spectra of Mrk 79 in the fitting region. The processed spectra (see Section 2.3) were fitted in two steps. We fitted the mean spectrum at first. During the fitting, the flux ratio of $[\text{O III}]\lambda\lambda 5007/\lambda 4959$ doublets was fixed to the theoretical value of 3. The shift and line width of the broad $\text{He II}\lambda 4686$ emission line were fixed to the best value measured in Section 2.3 because it's too weak to restrict the model. The rest of model parameters were allowed to vary. Then in the fitting of individual spectrum, we fixed the spectral index, the flux ratios of the narrow emission lines relative to $[\text{O III}]\lambda 5007$ to the corresponding values given by the best fit of the mean spectra. The spectra of Mrk 79 show weak features of Fe II

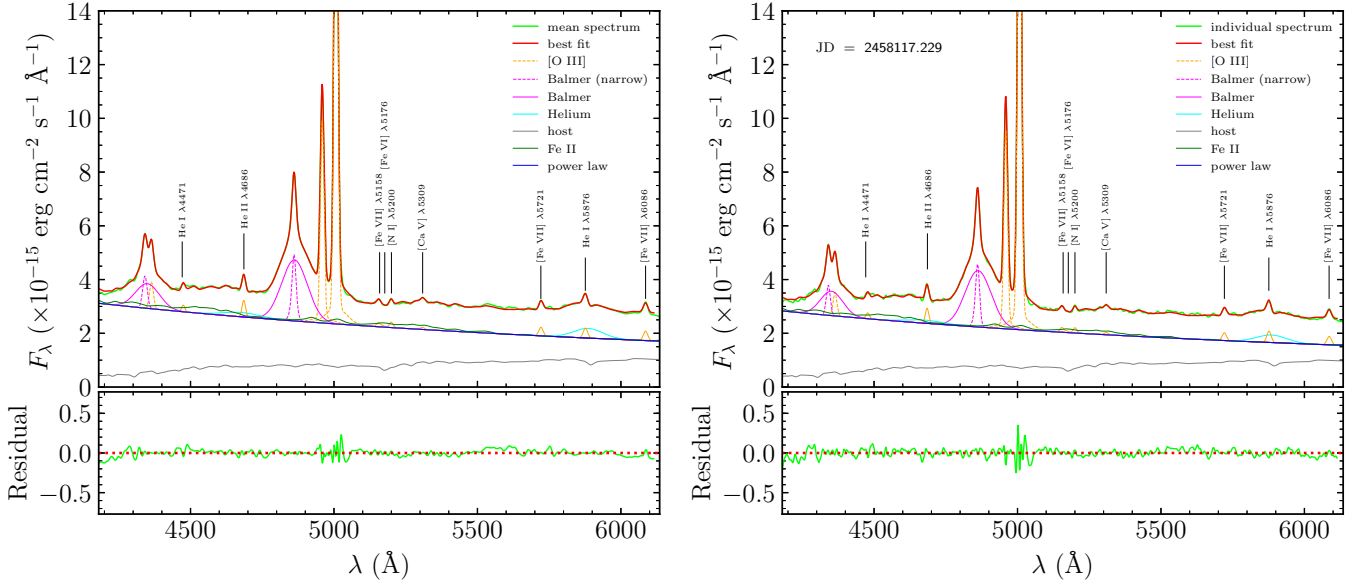


Figure 3. Multi-components fitting of (*left*) the mean spectrum and (*right*) an individual spectrum of Mrk 79. The top traces show the processed spectrum (lime, see Section 2.3) and the best-fit model (red), which is composed of AGN power-law continuum (blue), Fe II multiplets (green), host galaxy (gray), broad emission lines including H β λ 4861, H γ λ 4340 (magenta), He II λ 4686 and He I λ 5876 (cyan), and several narrow emission lines (orange). The bottom trace shows the residuals (lime).

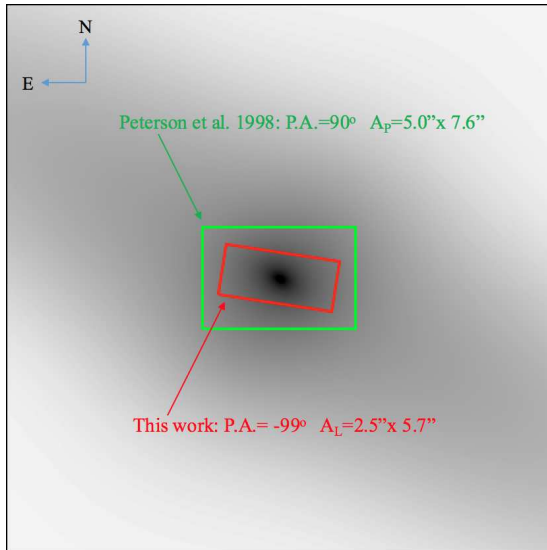


Figure 4. The best-fit model for host galaxy based on the two dimensional decomposition of the *HST* image (Kim et al. 2017). Extracted apertures of spectrum are overlaid in red rectangle (adopted by this work) and green rectangle (adopted by Peterson et al. 1998). P.A. is position angle of slit. Image is displayed on logarithmic stretch with $25'' \times 25''$.

multiplets, so we also fixed its width to the value fitted in the mean spectrum. In practice, this operation is reasonable since we have corrected the broadening of emission lines (see Section 2.3).

Using the fitting results, we calculated the revised mean and rms spectra after subtracting of the narrow emission lines, and over-plotted along with the original mean and rms spectra in Figure 2. Comparing revised mean spectrum (in red) with original mean spectrum (in blue), we found that the narrow emission lines are well fitted and subtracted. From Figure 2b, we found that the residuals of

[O III] λ 4959, 5007 almost disappear in the revised rms spectrum, minor residuals are comparable with mean errors (in dashed green-line).

3.3. Host galaxy

Mrk 79 was observed by the *HST* (*Hubble Space Telescope*) ACS/HRC (Advanced Camera for Surveys/High resolution channel) with F550M filter. Two-dimensional surface brightness decomposition of Mrk 79 was performed by Bentz et al. (2009a) and Kim et al. (2017) using the code GALFIT (Peng et al. 2002; Kim et al. 2008). Kim et al. (2017) recently analysed high-resolution *HST* images of 235 low-redshift Type 1 AGNs to study the structures of the host galaxy. We adopted the best-fit model for the host galaxy of Mrk 79 from Kim et al. (2017), which is shown in Figure 4. Bentz et al. (2009a) also analysed *HST* images of 35 RM AGNs to measure the contribution of host light to the total luminosity at 5100 \AA . They concluded the flux of host light at 5100 \AA for Mrk 79 is $F_{\text{host},A_P}[1+z] = 1.42 \times 10^{-15} \text{ erg s}^{-1} \text{ cm}^{-2} \text{ \AA}^{-1}$ within an aperture of $5.0'' \times 7.6''$ (A_P ; lime rectangle). In this work, the extraction aperture of spectrum is $2.5'' \times 5.7''$ with a position angle -99° (A_L ; red rectangle in Figure 4). Integrating the photons in the extraction apertures of $2.5'' \times 5.7''$ and $5.0'' \times 7.6''$, respectively, we obtained the ratio of total photons of the host galaxy in two apertures $A_L/A_P = 0.60$. Using this ratio and the host-galaxy flux $1.42 \times 10^{-15} \text{ erg s}^{-1} \text{ cm}^{-2} \text{ \AA}^{-1}$, we estimated the host-galaxy flux in our adopted extraction aperture for Mrk 79, which yields $F_{\text{host},A_L}[1+z] = 0.85 \times 10^{-15} \text{ erg s}^{-1} \text{ cm}^{-2} \text{ \AA}^{-1}$. The fitting of mean spectrum yields an average host-galaxy flux of $F_{\text{host}}[1+z] = (0.80 \pm 0.09) \times 10^{-15} \text{ erg s}^{-1} \text{ cm}^{-2} \text{ \AA}^{-1}$, where uncertainty 0.09 is the standard deviation estimated from the fitted host-galaxy components (Section 3.2). This flux is consistent

with the above estimate from *HST* image because measuring the flux contribution from the image has an uncertainty of $\sim 10\%$ (Bentz et al. 2013). This consistency indirectly shows that the spectral decomposition of Mrk 79 is robust and the host galaxy of Mrk 79 is well fit with a bulge, a bar, and a disk (see Kim et al. 2017).

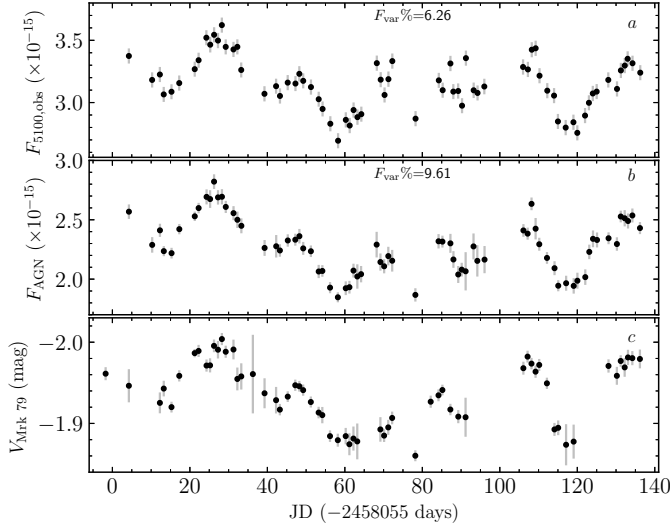


Figure 5. Comparison of light curves. Panels (a-c) are light curves of the observed continuum at 5100 Å (from the processed spectra), AGN continuum (from the featureless power law), and Mrk 79 photometry (see Section 3.4), respectively.

3.4. Light Curves

The light curves of AGN continuum at 5100 Å (F_{AGN}) and broad emission lines ($F_{\text{H}\beta}$ $\lambda 4861$, $F_{\text{H}\gamma}$ $\lambda 4340$, $F_{\text{He II } \lambda 4686}$, and $F_{\text{He I } \lambda 5876}$) were generated from the best-fit model (the featureless power law and the broad line components). Table 1 provides the data of these light curves along with the photometric light curve of Mrk 79. We also measured the fluxes of the host galaxy (F_{gal}) and [O III] $\lambda 5007$ ($F_{[\text{O III}]}$) from the best-fit model, and directly measured the light curve of continuum at 5100 Å ($F_{5100,\text{obs}}$, which is contaminated by the host galaxy) from the above processed spectra (see Section 2.3). We calculated the variability amplitude of the light curve by (see Rodríguez-Pascual et al. 1997)

$$F_{\text{var}} = \frac{(\sigma^2 - \Delta^2)^{1/2}}{\langle F \rangle} \quad (3)$$

and its uncertainty (Edelson et al. 2002)

$$\sigma_{F_{\text{var}}} = \frac{1}{F_{\text{var}}} \left(\frac{1}{2N} \right)^{1/2} \frac{\sigma^2}{\langle F \rangle}, \quad (4)$$

where $\langle F \rangle = N^{-1} \sum_{i=1}^N F_i$ is the average flux, F_i is the flux of the i -th observation of the light curve, N is the total number of observations, $\sigma^2 = \sum_{i=1}^N (F_i - \langle F \rangle)^2 / (N - 1)$, $\Delta^2 = \sum_{i=1}^N \Delta_i^2 / N$, and Δ_i is the uncertainty of F_i . Table 2 lists the statistics of the light curve.

We compared the light curves of F_{AGN} and $F_{5100,\text{obs}}$ (Figure 5a and 5b), and found that the light curve of F_{AGN} has the larger variability amplitude ($F_{\text{var}}\% = 9.61$) than the light curve of $F_{5100,\text{obs}}$ ($F_{\text{var}}\% = 6.26$). Which shows that the light curve of F_{AGN} has improved after removing the contamination of the host galaxy. Both light curves measured from the spectra are consistent with the photometric light curve of Mrk 79 (Figure 5c). This consistency shows that the stable comparison star can provide precise flux calibration of spectra.

We also checked the fluxes of the host galaxy and the [O III] $\lambda 5007$ (measured from the best-fit components) in Figure A2a and A2b, found that the both fluxes have similar apparent variation in the time domain, and found that the host-galaxy fluxes (11%) are more scatter than [O III] $\lambda 5007$ (5%). Similar phenomena are found in Mrk 382 by Hu et al. (2015). These measurement results are consistent with the considerations of spectroscopic observation in Section 2.1 (the third paragraph). That is monitoring the spectra of Mrk 79 in a relatively narrow slit (2.5'') contributes to increase the spectral resolution, but varying observing conditions cause the apparent variation in flux of the slightly extended components observed in the narrow slit (including the [O III] emission region and the host galaxy). The apparent variation in flux of the [O III] $\lambda 5007$ leads to the [O III] remaining in the rms spectrum, which supports the second scenario mentioned in Section 3.1.

In order to qualitatively study the apparent variation in flux of the host galaxy and the [O III] 5007, we have insight into the details of spectroscopy and flux calibration in Appendix A. Briefly, seeing is a major factor in responding to varying observing conditions, which could change from one exposure to the next. Two point sources (the comparison star and AGN) kept in a line parallel to the narrow slit (2.5''), the fractions of light loss due to varying seeing are identical (Figure A1), that is the stable comparison star can provide precise flux calibration of spectra (see figure 5 and accompanying statements). However, the slightly or very extended components in the same slit, the fractions of light loss due to varying seeing are less than the point source (Figure A1 of Appendix A). In practice, above analysis is consistent with seeing-induced aperture effects addressed by Peterson et al. (1995). Consequently, the calibrated fluxes of the slightly extended components should correlate with varying seeing; The host-galaxy fluxes should be more scatter than the [O III]'s fluxes with varying seeing, because the intrinsic size of the host galaxy is larger than the [O III] emission region. The elaborate analysis is provided in Appendix A. Ultimately, our measurement results in fluxes of the slightly extended components (i.e. Figure A2 and A3) from the spectral fitting productions are consistent with above analysis (details refer to Appendix A), this consistency demonstrates that the spectral fitting scheme performs correct decomposition of multi-components.

Table 1. Light curves of continuum at 5100 Å and broad emission lines for Mrk 79

JD–2450000	V-band (mag)	JD–2450000	F_{AGN}	$F_{H\gamma}$	$F_{He II}$	$F_{H\beta}$	$F_{He I}$
8053.25	-1.96 ± 0.01	8059.26	2.57 ± 0.06	1.03 ± 0.05	3.26 ± 0.31	2.65 ± 0.04	4.71 ± 0.17
8059.25	-1.95 ± 0.02	8065.27	2.29 ± 0.07	1.03 ± 0.04	2.07 ± 0.31	2.60 ± 0.04	4.73 ± 0.17
8067.26	-1.93 ± 0.01	8067.27	2.41 ± 0.06	0.98 ± 0.04	2.49 ± 0.29	2.64 ± 0.04	4.87 ± 0.16
8068.25	-1.94 ± 0.01	8068.27	2.24 ± 0.04	0.96 ± 0.04	1.64 ± 0.27	2.56 ± 0.03	4.71 ± 0.12
8070.25	-1.92 ± 0.01	8070.27	2.22 ± 0.05	0.95 ± 0.04	0.95 ± 0.27	2.54 ± 0.03	4.71 ± 0.14

NOTE—V-band is photometric data (instrumental magnitude), F_{AGN} is AGN continuum at 5100 Å in units of 10^{-15} erg s $^{-1}$ cm $^{-2}$ Å $^{-1}$, $F_{H\gamma}$ and $F_{H\beta}$ are the fluxes of H γ λ 4340 and H β λ 4861 in units of 10^{-13} erg s $^{-1}$ cm $^{-2}$, $F_{He II}$ and $F_{He I}$ are the fluxes of He II λ 4686 and He I λ 5876 in units of 10^{-14} erg s $^{-1}$ cm $^{-2}$. This table is available in its entirety in machine-readable form.

Table 2. Statistics of light curve for Mrk 79 in this campaign

Time Series	$F_{5100,obs}[1+z]$	$F_{AGN}[1+z]$	$F_{H\gamma}[1+z]$	$F_{He II}[1+z]$	$F_{H\beta}[1+z]$	$F_{He I}[1+z]$
Mean flux	3.22 ± 0.21	2.33 ± 0.23	1.00 ± 0.10	2.63 ± 1.21	2.61 ± 0.14	4.64 ± 0.42
F_{var} (%)	6.26 ± 0.57	9.61 ± 0.88	8.53 ± 0.92	45.37 ± 4.06	5.33 ± 0.48	8.28 ± 0.85

NOTE—The mean flux $F_{5100,obs}[1+z]$ in units of 10^{-15} erg s $^{-1}$ cm $^{-2}$ Å $^{-1}$, the mean flux of other time series have same units with Table 1.

Table 3. Summary of previous RM results of Mrk 79

Epoch (JD: days)	$F_{obs}[1+z]$	$F_{host}[1+z]$	$F_{AGN}[1+z]$	L_{5100} (erg s $^{-1}$)	H β Lags (days)	Ref.
2447838–2448044	6.96 ± 0.15	1.42 ± 0.07	5.54 ± 0.18	$(3.45 \pm 0.12) \times 10^{43}$	$9.0^{+8.3}_{-7.8}$	(1,2)
2448193–2448393	8.49 ± 0.16	1.42 ± 0.07	7.07 ± 0.19	$(4.41 \pm 0.11) \times 10^{43}$	$16.1^{+6.6}_{-6.6}$	(1,2)
2448905–2449135	7.40 ± 0.16	1.42 ± 0.07	5.98 ± 0.19	$(3.73 \pm 0.12) \times 10^{43}$	$16.0^{+6.4}_{-5.8}$	(1,2)
2458059–2458192	3.22 ± 0.22	0.80 ± 0.09	2.33 ± 0.23	$(1.45 \pm 0.14) \times 10^{43}$	$3.49^{+0.62}_{-0.60}$	(3)

NOTE—References: (1) Peterson et al. (1998); (2) Bentz et al. (2013); (3) This work, H β lag from Table 4.

The units of $F_{obs}[1+z]$, $F_{host}[1+z]$, and $F_{AGN}[1+z]$ are 10^{-15} erg s $^{-1}$ cm $^{-2}$ Å $^{-1}$.

Table 4. RM measurements of Mrk 79 from the present campaign

Lines	Line vs. F_{AGN}			Mean spectra		rms spectra		VP ($\times 10^7 M_{\odot}$)	VP ($\times 10^7 M_{\odot}$)
	τ_{cent}	τ_{peak}	τ_{max}	FWHM (km s $^{-1}$)	σ_{line} (km s $^{-1}$)	FWHM (km s $^{-1}$)	σ_{line} (km s $^{-1}$)		
(1)	(2)	(3)	(4)	(5)	(6)	(7)	(8)	(9)	(10)
H γ	$2.43^{+1.55}_{-0.88}$	$2.32^{+1.00}_{-1.17}$	0.79	6730 ± 312	2739 ± 216	10757 ± 377	3679 ± 137	$2.15^{+1.38}_{-0.80}$	$0.64^{+0.41}_{-0.24}$
He II	$-0.05^{+0.50}_{-0.40}$	$0.21^{+0.28}_{-0.77}$	0.86	—	—	9585 ± 815	4003 ± 121	—	—
H β	$3.49^{+0.62}_{-0.60}$	$2.36^{+2.03}_{-0.49}$	0.83	6539 ± 154	2660 ± 136	8431 ± 621	3458 ± 132	$2.91^{+0.54}_{-0.52}$	$0.82^{+0.16}_{-0.15}$
He I	$4.39^{+1.26}_{-1.12}$	$4.43^{+1.73}_{-1.80}$	0.69	6124 ± 223	2470 ± 156	8182 ± 598	3345 ± 134	$3.21^{+0.95}_{-0.85}$	$0.96^{+0.28}_{-0.25}$

Table 4 continued

Table 4 (*continued*)

Lines	Line vs. F_{AGN}			Mean spectra		rms spectra			
	τ_{cent}	τ_{peak}	r_{max}	FWHM (km s^{-1})	σ_{line} (km s^{-1})	FWHM (km s^{-1})	σ_{line} (km s^{-1})	VP ($\times 10^7 M_{\odot}$)	VP ($\times 10^7 M_{\odot}$)
(1)	(2)	(3)	(4)	(5)	(6)	(7)	(8)	(9)	(10)

NOTE—The Lags (τ_{cent} and τ_{peak}) are in the rest frame. The VPs of Col. (9) are calculated using the measurements of Col. (2) and Col. (5), and Col. (10) are calculated using the measurements of Col. (2) and Col. (8).

3.5. Optical luminosity

Using the light curve of AGN continuum at 5100 Å generated from the best-fit power law, we obtained the mean flux of $F_{\text{AGN}}[1+z] = (2.33 \pm 0.23) \times 10^{-15} \text{ erg s}^{-1} \text{ cm}^{-2} \text{ \AA}^{-1}$, which corresponds the monochrome luminosity of $L_{5100} = (1.45 \pm 0.14) \times 10^{43} \text{ erg s}^{-1}$ in the present epoch. Before this RM campaign, three-season RM campaigns for Mrk79 were finished by Peterson et al. (1998), the data were updated and published in a series works (e.g., Peterson et al. 2004; Zu et al. 2011; Bentz et al. 2013). Primary parameters along with values are summarised in Table 3, where the values of H β lags quoted in Table 3 are compiled from latest result of Bentz et al. (2013). Comparing these fluxes ($F_{\text{AGN}}[1+z]$) for the host galaxy correction, we found that Mrk 79 is seeming to come out the faint state during the monitoring period. The mean flux approximates a magnitude fainter than previous record holder. We checked the historical data (Peterson et al. 1998), and found that the highest luminosity state of Mrk 79 appeared at JD \sim 2448400 days. Similar to the famous NGC 5548 (Lu et al. 2016), the huge variation of AGN continuum benefit us to (1) investigate the variation of the BLR similar to NGC 5548 (Lu et al. 2016); (2) construct the Radius–Luminosity relationship of Mrk 79, similarly see $R_{\text{BLR}} - L_{5100}$ relationship of NGC 5548 (Lu et al. 2016; Pei et al. 2017).

3.6. Line profile measurements

The broad emission lines including H γ λ 4340, H β λ 4861, and He I λ 5876 were covered in our spectral fitting window. Hence, we measured the velocity widths of these broad emission lines from the best-fit model. Using Equation 1 and 2, we obtained the mean and rms spectrum of these broad lines at first. They velocity widths (FWHM & σ_{line}) are used as the optimum values. As adopted in Section 3.1, to estimate the corresponding errors, we generated 200 mean and rms spectra (realizations) from 200 randomly chosen subsets of the spectra, and measured all velocity widths from simulated realizations. Then we used the standard deviations as errors of the optimum values. Whittle (1992) obtained [O III] λ 5007 width (FWHM= 350 km s^{-1}) of Mrk 79 from high resolution spectrum. Comparing this width to those from our spectra (FWHM= 900 km s^{-1}), we obtained a broadening of 829 km s^{-1} . After correcting the broadening, we listed the widths of the broad lines in Table 4. In spectral fitting, the velocity width of broad He II λ 4686 line was fixed to the value estimated from rms spectrum (see Section 3.1), therefore we only give its velocity width from rms spectrum in

Table 4.

3.7. Lags of the broad emission lines

We measured the reverberation lags of the broad emission lines (H β λ 4861, H γ λ 4340, He II λ 4686, and He I λ 5876) with respect to the continuum variation (F_{AGN}), using the standard interpolation cross-correlation function (ICCF) method (Gaskell & Sparke 1986; Gaskell & Peterson 1987; White & Peterson 1994). The reverberation lags are usually measured from peak (τ_{peak}) and centroid (τ_{cent}) of the ICCF, where τ_{peak} corresponds the maximum correlation coefficient r_{max} , and τ_{cent} is measured around the peak above a typical value ($r \geq 0.8 r_{\text{max}}$). The uncertainties of τ_{peak} and τ_{cent} were obtained using the Monte Carlo “flux randomization and random subset sampling” method described by Peterson et al. (1998) and Peterson et al. (2004). The Monte Carlo simulations were run with 5000 realizations, and the cross-correlation peak and centroid distribution (CCPD and CCCD) were created from the generated samples. The uncertainties of τ_{peak} and τ_{cent} were then calculated from the CCPD and CCCD, respectively, with a 68.3% confidence level (1σ).

Table 4 lists the lags of the broad emission lines including τ_{cent} , τ_{peak} , and the maximum cross correlation coefficients (r_{max}). In the low luminosity state of Mrk 79 (see Section 3.5), the lag of H β λ 4861 relative to the continuum variation is significant shorter than the results of early RM campaigns (see Table 3). This is similar to the finding in better-observed NGC 5548 that the BLR size shortens with luminosity decreasing (e.g., Peterson et al. 1999, 2002; Bentz et al. 2007; De Rosa et al. 2018; Lu et al. 2016; Kriss et al. 2019). In addition, the lag of He II λ 4686 relative to the continuum variation approximates zero, which is consistent with other objects (e.g., Mrk 1511, see Barth et al. 2013).

3.8. Velocity-resolved reverberation mapping

The BLR is an extended region and the velocity of the gas is most likely a function of radii. The BLR gas in different radii should respond to the continuum variations on slightly different delays. The reverberation lags measured between the continuum variations and the total fluxes of the broad emission lines in Table 4 represent the radii averaged by the emissivity function of the BLR. Based on a single broad emission line, velocity-resolved reverberation mapping was widely used to reveal the kinematic signatures of the BLR in many ANGs (e.g., Denney et al. 2009a, 2010; Bentz et al.

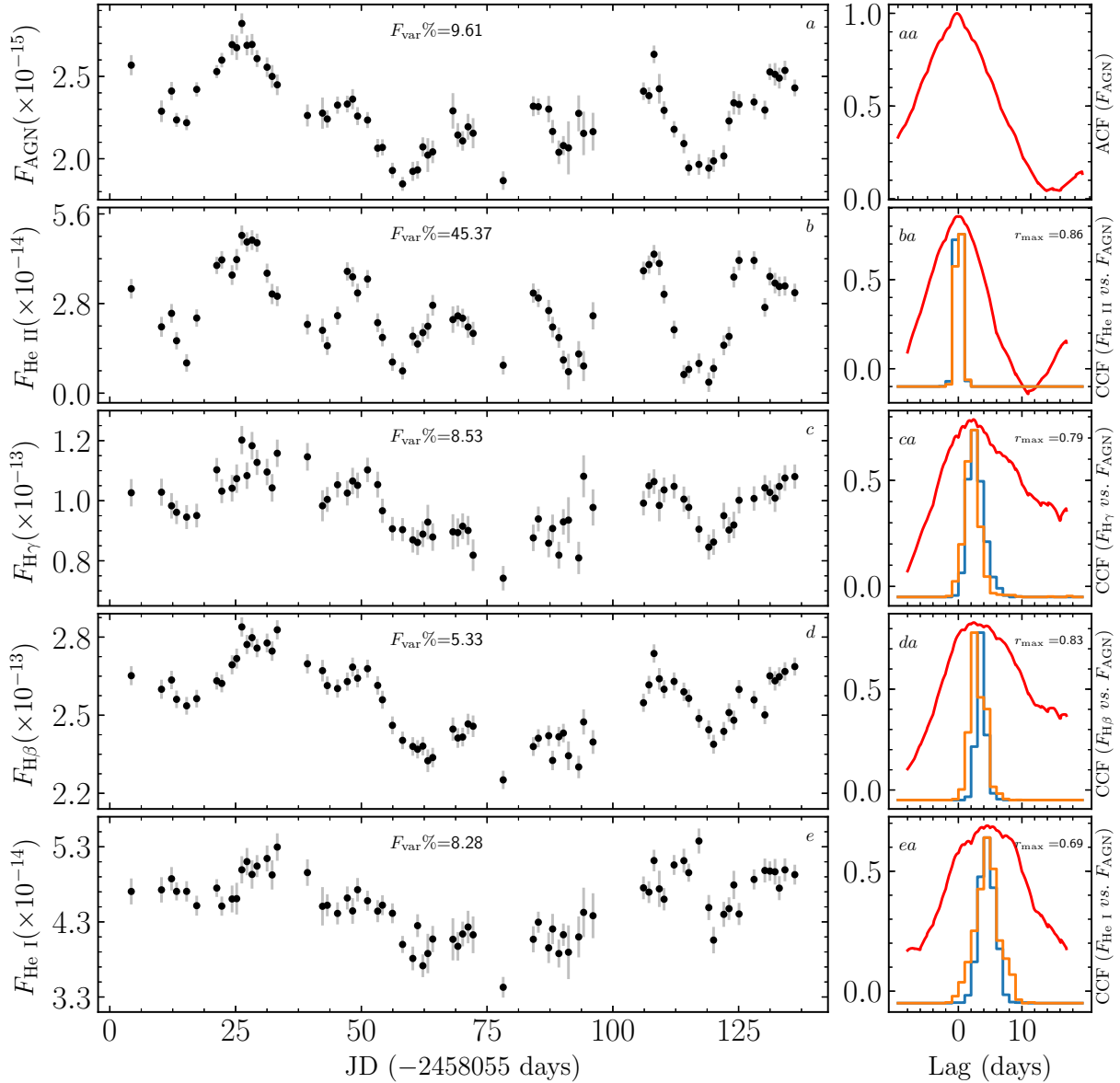


Figure 6. Light curves and the results of cross correlation analysis. The left panels (a-e) are the light curves of AGN continuum at 5100 \AA and the broad emission lines calculated from the best-fit component. The right panels (aa-*ea*) correspond to the ACF of continuum and the CCF between the light curves of broad emission lines (b-e) and the continuum variation (a), respectively. We noted the variability amplitude $F_{\text{var}}\%$ in panel of light curves, and noted the maximum cross-correlation coefficient (r_{max}) in panel of CCF. The units of F_{AGN} and emission lines (including Helium and Balmer) are $\text{erg s}^{-1} \text{cm}^{-2} \text{\AA}^{-1}$ and $\text{erg s}^{-1} \text{cm}^{-2}$, respectively.

2009b, 2010; Barth et al. 2011a,b; Grier et al. 2013; Du et al. 2016; Lu et al. 2016; Pei et al. 2017; De Rosa et al. 2018; Zhang et al. 2019). Although three RM-campaign of Mrk 79 have been performed before the present campaign, the study of the BLR kinematics is still blank. In this section, we constructed the velocity-resolved lag profiles of the broad emission lines (H β λ 4861, H γ λ 4340, He II λ 4686, and He I λ 5876). Following previous method (e.g., Denney et al. 2009b; Lu et al. 2016; Pei et al. 2017), our procedure is as follows. At first, we calculated the rms spectrum of these broad lines, as illustrated in Figure 7 (top panels). Then we selected a wavelength range and divided the rms profiles of broad emission lines into nine uniformly spaced bins (each

bin has same velocity width $\sim 1300 \text{ km s}^{-1}$)¹. The light curves of each bin were finally obtained by just integrating the fluxes in the bin, corresponding light curves were shown in the left panels of Figures (B4, B5, B6, B7) and were numbered with Bin number (i.e., Bin 1 to 9 from blue wing, line core to red wing of broad lines). Using Equation (3), we calculated variability amplitudes F_{var} of the velocity-resolved light curves and noted these values in the left panels of Fig-

¹ The instrumental broadening (ψ) is 829 km s^{-1} for adopting $2.5''$ slit. The average broadening in each velocity bin is significantly smaller than bin width ($\sim 1300 \text{ km s}^{-1}$), which means that the instrumental broadening has a negligible impact on our analysis.

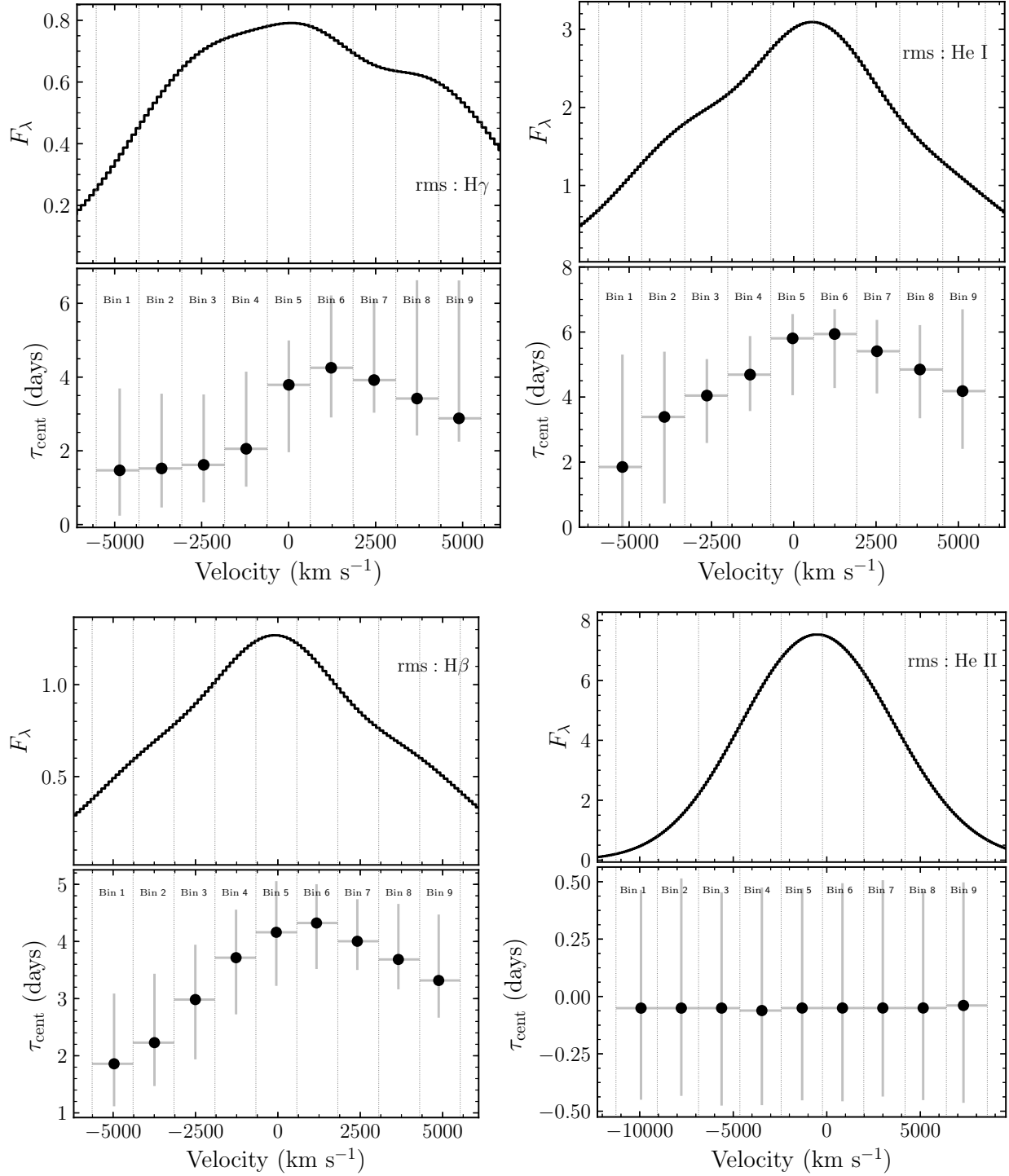


Figure 7. The rms profiles (top panels) and velocity-resolved lag profiles (bottom panels) of the broad H γ , H β , He I, and He II lines. The vertical dash-lines are the edges of the velocity bins. Each bin is labeled with Bin number (Bin 1–9), which is one-to-one correspondence with Figures (B4, B5, B6, B7).

ures (B4, B5, B6, B7). The reverberation lag of each bin and associated uncertainty were determined using same procedures as described in Section 3.7. The results of cross correlation analysis are shown in the right panels of Figures (B4, B5, B6, B7).

Bottom panels of Figure 7 show the velocity-resolved lag profiles (VLPs) of the broad H β λ 4861, H γ λ 4340,

He II λ 4686, and He I λ 5876 emission lines. The vertical dash-lines are the edges of the velocity bins. Each bin is labeled with Bin number, which is one-to-one correspondence with Figures (B4, B5, B6, B7). For the VLP of He II λ 4686, the absolute value of 9 velocity-dependent delays are less than 0.5 day, which is shorter than median sampling of 1.0 day. A higher sampling is necessary to construct

clear VLP of broad He II $\lambda 4686$ line by decreasing the errors. The VLPs of H γ $\lambda 4340$, H β $\lambda 4861$, and He I $\lambda 5876$ almost have same kinematic signatures. They demonstrate that the high-velocity gas in the wings exhibits a shorter lag than the low-velocity gas. This is consistent with the virial nature of gas motion in the BLR (Bentz et al. 2009b; Grier et al. 2013), that is gas kinematics of the BLR during the monitoring period is dominated by Keplerian gas motion. However, the lag in the red wing is slightly larger than the lag in the blue wing, and the largest delay response occurs in the red side of the line core (i.e., Bin6; $\sim +1500$ km s $^{-1}$) for these broad emission lines. Similar signature has been seen in NGC 3227 (see Figure 3 of Denney et al. 2009a). This is a signature of outflow gas motion (Bentz et al. 2009b; Grier et al. 2013). These complicated signatures should suggest that the BLR of Keplerian motion in Mrk 79 probably exists the outflow gas motion during the monitoring period.

3.9. Black hole mass and accretion rates

Using the RM measurements of the broad emission lines, we determined BH mass of Mrk 79 by equation

$$M_{\bullet} = f_{\text{BLR}} \frac{c\tau_{\text{BLR}} V_{\text{BLR}}^2}{G} \equiv f_{\text{BLR}} \text{VP}, \quad (5)$$

where $c\tau_{\text{BLR}}$ is the size of the BLR, c is the speed of light, τ_{BLR} is the lag of the broad emission line with respect to the continuum variation, G is the gravitational constant, V_{BLR} (i.e., FWHM or σ_{line}) is the velocity width of the broad emission lines, and VP is commonly called the virial product. The coefficient f_{BLR} called virial factor depends on the geometry, kinematics, and inclination of the BLR.

We first calculated VP based on the different broad emission lines and tabulated results in Table 4. Graham et al. (2011) the first evaluated the virial factor f_{BLR} taking into account the morphology of the host galaxies, and found that the factor f_{BLR} for barred galaxies is three times lower than that for non-barred galaxies. Ho & Kim (2014) reevaluated the factor f_{BLR} for the RM AGN sample taking into account the bulge type of the host galaxies and found that the systematic difference in f_{BLR} between barred and non-barred galaxies qualitatively resembles the dependence on bulge type. Ho & Kim (2014) suggested that pseudo-bulge notably has a lower f_{BLR} than in classical bulge. For FWHM measured from mean spectrum, $f_{\text{BLR}} = 0.5 \pm 0.2$ for pseudo-bulges, whereas $f_{\text{BLR}} = 1.3 \pm 0.4$ for classical bulges. For σ_{line} measured from rms spectrum, $f_{\text{BLR}} = 3.2 \pm 0.7$ for pseudo-bulges, whereas $f_{\text{BLR}} = 6.3 \pm 1.5$ for classical bulges. The host galaxy of Mrk 79 has a classical bulge (Kim et al. 2017). Based on broad H β line, multiplying virial factor $f_{\text{BLR}} = 1.3 \pm 0.4$ and $f_{\text{BLR}} = 6.3 \pm 1.5$ to $\text{VP}|_{\text{FWHM}_{\text{H}\beta}}$ ($= 2.91_{-0.52}^{+0.54} \times 10^7 M_{\odot}$) and $\text{VP}|_{\sigma_{\text{H}\beta}}$ ($= 0.82_{-0.15}^{+0.16} \times 10^7 M_{\odot}$), we obtained $M_{\bullet} = 3.79_{-1.35}^{+1.36} \times 10^7 M_{\odot}$ and $5.13_{-1.55}^{+1.57} \times 10^7 M_{\odot}$, respectively. Our measurement of BH mass for Mrk 79 is consistent with previous results (see Peterson et al. 1998; Bentz et al. 2013). The bulge of Mrk 79 has a stellar velocity dispersion (130 ± 12) km s $^{-1}$ (Nelson et al. 2004). Using the latest $M_{\bullet} - \sigma_{*}$ relation Kormendy & Ho (2013), we obtained $M_{\bullet}|\sigma_{*} = 4.68 \times 10^7 M_{\odot}$ with the scatter 0.34

dex, which is consistent with estimates from $\text{VP}|_{\sigma_{\text{H}\beta}}$ and $\text{VP}|_{\text{FWHM}_{\text{H}\beta}}$.

Based on the standard model of accretion disk, the dimensionless accretion rates are related to the 5100 Å luminosity and BH mass via (Du et al. 2015)

$$\dot{M} = \frac{\dot{M}_{\bullet}}{L_{\text{Edd}} c^{-2}} = 20.1 \left(\frac{\ell_{44}}{\cos i} \right)^{3/2} M_7^{-2}, \quad (6)$$

where \dot{M}_{\bullet} is the mass accretion rates, L_{Edd} is the Eddington luminosity, c is the speed of light, $\ell_{44} = L_{5100}/10^{44}$ erg s $^{-1}$ is optical luminosity at 5100 Å, $M_7 = M_{\bullet}/10^7 M_{\odot}$ is BH mass, $\cos i$ is the cosine of the inclination of the accretion disk. $i = 24$ degrees for Mrk 79 (Gallo et al. 2011). Using $M_{\bullet} = 5.13_{-1.55}^{+1.57} \times 10^7 M_{\odot}$ and $L_{5100} = (1.45 \pm 0.14) \times 10^{43}$ erg s $^{-1}$, we obtained accretion rates $\dot{M}_{\bullet} = (0.05 \pm 0.02) L_{\text{Edd}} c^{-2}$, indicating that Mrk 79 is a sub-Eddington accreting AGN.

4. DISCUSSION

4.1. Indirect evidence of the BLR as a disk wind

On the one hand, UFOs and warm absorbers are identified in term of X-ray spectrum for Mrk 79 (Tombesi et al. 2010, 2011; Gallo et al. 2011), but their geometries remain unclear (Parker et al. 2018). We don't know whether blueshifted UV absorbers/emitters exist in Mrk 79 in absence UV spectrum. In Section 3.1, we detected marginal blueshift of the broad He II $\lambda 4686$ line with velocity of ~ 450 km s $^{-1}$, which indicates an outflow of high-ionization gas (e.g., He II emitters). But it is significantly slower than the velocity of UFOs ($0.016 V_{\text{UFOs, out}}$). As suggestion of disk wind model (Murray et al. 1995; O'Brien et al. 2005; Tombesi et al. 2013), this result may attribute to a possibility that the X-ray outflow could be the source of some of the BLR gas. In addition, based on the velocity-resolved lag profiles of broad He I $\lambda 5876$, H β $\lambda 4861$, and H γ $\lambda 4340$ lines (Section 3.8), we found that low-ionization gas of the BLR exhibits the outflowing signature during the monitoring period. Meanwhile, we found that Mrk 79 is similar to NGC 3227 (see Section 1) in some aspects. For example, (1) UFOs and warm absorbers were detected in both AGNs; (2) the low-ionization BLR of both AGNs exhibit the outflowing component (see Section 3.8 and Denney et al. 2010). While, based on velocity-resolved RM, we do not find that the BLR doubtlessly exhibits an outflowing component for normal AGN (i.e., no disk wind) so far. These findings may indicate that the outflowing BLR could be associated with disk wind, and may support the notion that disk wind could be the source of some of the BLR gas as suggested by O'Brien et al. (2005). All of these phenomenons including UFOs, warm absorbers, and the kinematics of the high- and low-ionization BLR, may provide an indirect evidence that the BLR of Mrk 79 probably originates from disk wind. However, simultaneous observations of multi-band spectra are necessary to further constrain this speculation.

It should be noted that, NGC 3227 as one of candidates of UFOs, the outflowing BLR in 2007 (Denney et al. 2010) turns to virialized BLR in 2012. De Rosa et al. (2018) suggested that the most likely reason for this change is that the

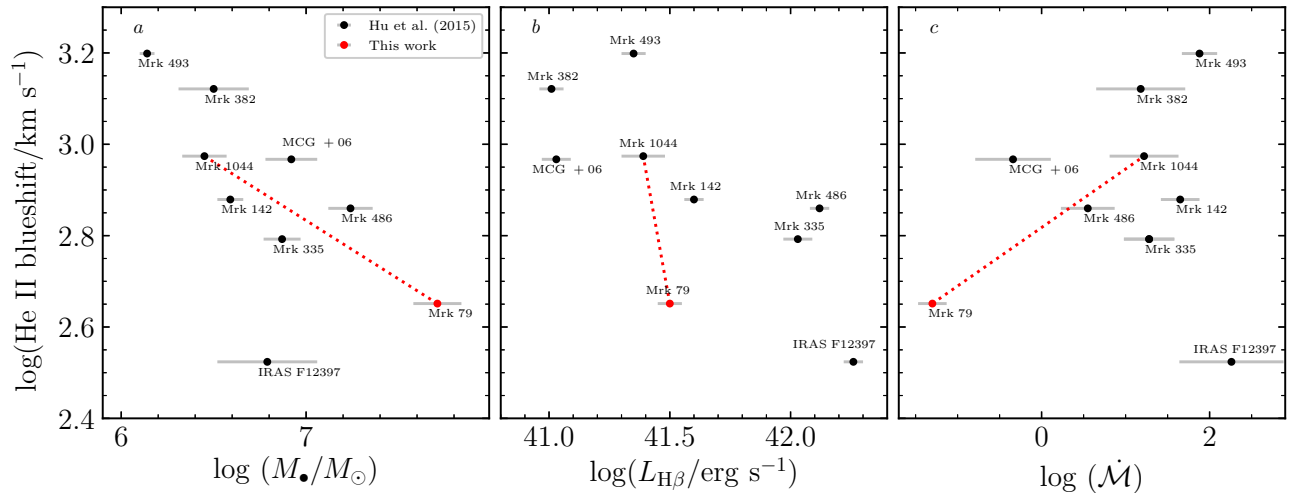


Figure 8. Relation between blueshift velocity of the broad He II $\lambda 4686$ line and AGN properties including BH mass, luminosity of the broad H β line, and accretion rates. Disk wind was just detected in Mrk 79 and Mrk 1044, they are connected in a dashed line.

BLR structure is probably complex and consists of multiple components—a disk and a wind. In this case, the decelerating and cooling outflow may gradually fall and turn to virialization, or it could be real intrinsically that the BLR kinematics are variable on the dynamical timescale as we saw in NGC 5548 (Lu et al. 2016; Kriss et al. 2019; De Rosa et al. 2018; Xiao et al. 2018). Therefore, the different BLR kinematics will be observed from the different campaigns.

On the other hand, when NGC 5548 is seeming to come out of faint state (e.g., De Rosa et al. 2018; Pei et al. 2017; Kriss et al. 2019), the broad emission lines failed to respond to variations in the continuum flux as the BLR ‘holiday’. Dehghanian et al. (2019) argued that X-ray absorption (observed by Mehdipour et al. 2016), produced transient obscurer, was present throughout the BLR ‘holiday’ of NGC 5548. Based on the X-ray and UV band monitoring of NGC 5548, Kriss et al. (2019) combined the observational facts including the obscurer and the departure of NGC 5548’s BLR from the radius–luminosity relationship (Peterson et al. 2002; Pei et al. 2017; De Rosa et al. 2018), and suggested that the obscurer is a manifestation of a disk wind launched in the brightening state. Coincidentally, what has been happening in better-studied NGC 5548 seems to have been happening in Mrk 79 as well. Both are seeming to come out of faint states, the H β lags are too short for the low luminosity state, and both are suspected of triggering disk wind. Unfortunately, we don’t have UV or X-ray spectra of Mrk 79.

It is worth noting that outflow of RQ AGN should be jointly triggered and controlled by central gravity and magnetic or (and) radiation pressure. In this case, the velocity of outflow should anticorrelate with BH mass, and positively correlate with magnetic or (and) radiation pressure. We compiled blueshifted velocity of the broad He II $\lambda 4686$ emission line from Hu et al. (2015) and this work, and investigated relationship between the blueshifted velocity of He II $\lambda 4686$ emitters and AGN properties including BH mass, luminosity of broad H β line (which is used as proxy of UV luminosity), and accretion rates in Figure 8. It should be noted that, in

this small sample, disk wind was only detected in Mrk 79 and Mrk 1044 (Parker et al. 2018). This sample shows a possible trend that the blueshifted velocity of He II emitters are anticorrelated with BH mass, which may suggest that central gravity plays a potential role on the terminal velocity of outflow. While we cannot see clear trend between blueshifted velocity of He II emitters and the rest of AGN properties (Figure 8b and 8c). An larger sample is necessary to responsibly investigate these relations. On the other hand, based on the results of 18 RM-campaigns of NGC 5548, Lu et al. (2016) recently found that the BLR size (τ_{BLR}) follows the variation of optical luminosity in the long-term timescale for NGC 5548 but with a time delay ~ 3 yr (also see Kriss et al. 2019), and implied the potential role of radiation pressure. Mrk 79 is monitored by 4 RM campaigns so far (including this work), nevertheless, more and dense RM campaigns are necessary to investigate this nature.

In addition, many possible origins of the BLR are developed besides the above case. For example, a series of works suggested that part of the BLR gas (or broad emission line) originate from the outer region of accretion disk (e.g., Collin-Souffrin 1987; Collin-Souffrin & Dumont 1990), but this scenario only produces low-ionization emission lines; Wang et al. (2017) modelled H β profile using dynamical model of different type clouds and suggested that tidally disrupted clumps from the torus may represent the source of the BLR; Czerny & Hryniewicz (2011) suggested that the BLR is a failed dusty wind from the outer accretion disk (also see Czerny et al. 2017); Baskin & Laor (2018) suggested the BLR originate from the dusty inflated accretion disk (see Figure 13 of Baskin & Laor 2018). However, whether these possible origins of the BLR are an intermediate state (phase) of multiphase disk wind should be studied in the future.

4.2. Radius–Luminosity relation

Many works focused on investigating the kinematics of the BLR in NGC 5548, and constructed its $R_{\text{BLR}} - L_{5100}$ relationship (Peterson et al. 2004; Bentz et al. 2007; Denney et al. 2010; Lu et al. 2016; Pei et al. 2017;

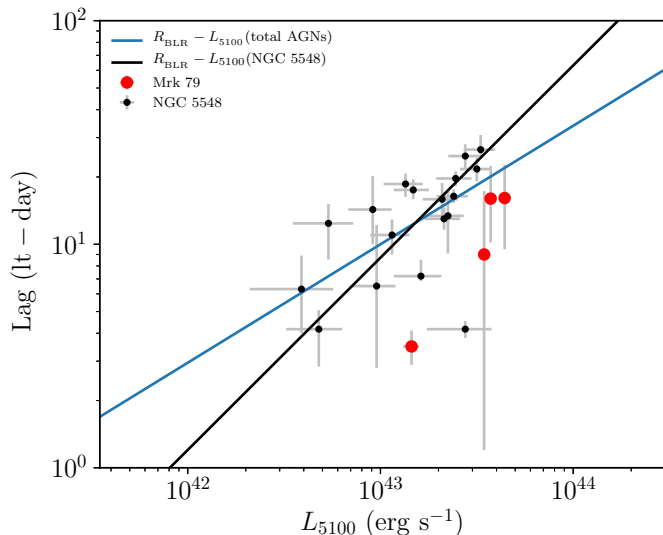


Figure 9. The $R_{\text{BLR}} - L_{5100}$ relation of Mrk 79 (red circles) along with NGC 5548 (black circles). Canonical $R_{\text{BLR}} - L_{5100}$ relationship (blue line) is taken from Bentz et al. (2013). The $R_{\text{BLR}} - L_{5100}$ relationship (black line) of NGC 5548 is taken from Lu et al. (2016).

De Rosa et al. 2018). Comparing the observation features of Mrk 79 in the past RM campaigns (see Section 3) with NGC 5548, we seemingly saw another ‘NGC 5548-like’ AGN in some aspects. For example, (1) the velocity widths of broad emission lines (such as $H\beta$ line) are very broad ($> 4000 \text{ km s}^{-1}$), that is they are broad-line Seyfert galaxy; (2) They have a classical bulge in the host galaxy (Kim et al. 2017); (3) Their BLR size and optical luminosity exhibit large variation (see Table 3; Lu et al. 2016; Kriss et al. 2019). Mrk 79 is expected to be a new candidate can be used to construct another $R_{\text{BLR}} - L_{5100}$ relationship of individual object because of enormous change of AGN continuum and the BLR size (Table 3). Figure 9 presents the canonical $R_{\text{BLR}} - L_{5100}$ relationship (slope=0.53) from Bentz et al. (2013) along with $R_{\text{BLR}} - L_{5100}$ relationship of NGC 5548 (slope=0.86, Lu et al. 2016). Black dots with error bars display the $R_{\text{BLR}} - L_{5100}$ relation of NGC 5548 reverberation, red circles with error bars display the $R_{\text{BLR}} - L_{5100}$ relation of Mrk 79 reverberation. We found that the current $R_{\text{BLR}} - L_{5100}$ relation of Mrk 79 deviates from the canonical $R_{\text{BLR}} - L_{5100}$ relationship (blue line) and NGC 5548’s $R_{\text{BLR}} - L_{5100}$ relationship (black line).

We noted that the previous works have described how the BLR radius in an individual object changes as the mean optical luminosity varies with time (e.g., Baldwin et al. 1995; Peterson et al. 1999, 2002). Based on the NGC5548’s results of 13-season RM campaigns, Peterson et al. (2002) found that the observed relation between the BLR radius and the luminosity in an individual AGN (Figure 5 of Peterson et al. 1999 and Figure 3 of Peterson et al. 2002) is consistent with the prediction of the simple photoionization equilibrium model. However, the latest studies found that (1) the BLR radius correlates with the averaged luminosity of AGN but with a delay, and this delay coincides with the BLR’s dynamical timescale (Ulrich et al. 1991; Lu et al. 2016; Kriss et al. 2019); (2) The shortened $H\beta$ lags correlate with the accretion

rates of AGN (e.g., Du et al. 2018). These results may imply that the BLR physics is probably complicated, the evolution of the BLR structure and kinematics may change the correlation between the BLR radius and luminosity of AGN predicted by photoionization equilibrium model. It is possible that comparing the $R_{\text{BLR}} - L_{5100}$ relationships of different AGNs (e.g., NGC 5548, Mrk 79 and so on) in the near future and investigating their similarities and differences could help us to understand the scatter (~ 0.3 dex, see Bentz et al. 2013; Du et al. 2018; Grier et al. 2017) of canonical $R_{\text{BLR}} - L_{5100}$ relationship.

5. SUMMARY

We developed an monitoring project to investigate the kinematics of the BLR in AGN with UFOs and explore potential connection between the BLR and disk wind. This is the first result from a new RM-campaign of Mrk 79, which was undertaken by Lijiang 2.4-m telescope (LJT+YFOSC). Spectral fitting scheme was adopted to remove the host-galaxy component from spectrum and improve the measurement quality of light curves. Reverberation analysis of several broad emission lines ($H\beta$ $\lambda 4861$, $H\gamma$ $\lambda 4340$, He II $\lambda 4686$, and He I $\lambda 5876$) are carried out. Based on the present campaign, We obtained the following results.

1. Mrk 79 is seeming to come out the faint state, the average flux of AGN at 5100 \AA approximates a magnitude fainter than previous record holder. We found that the variability amplitudes of the broad emission lines meet $F_{\text{var, He II}} > F_{\text{var, H}\gamma} > F_{\text{var, He I}} \geq F_{\text{var, H}\beta}$ relation.
2. High-ionization line of He II $\lambda 4686$ has a marginal blueshift with velocity $\sim 450 \text{ km s}^{-1}$, which indicates an outflow of high-ionization gas.
3. We successfully measured the time delays of the broad $H\beta$ $\lambda 4861$, $H\gamma$ $\lambda 4340$, He II $\lambda 4686$, and He I $\lambda 5876$ emission lines with respect to the continuum variation. The optimum lags of $H\gamma$ $\lambda 4340$, $H\beta$ $\lambda 4861$, and He I $\lambda 5876$ lines marginally show a ionization stratification of the BLR. The lag of He II $\lambda 4686$ line approximates zero, which is consistent with previous results.
4. We simultaneously obtained the velocity-resolved lag profiles of the broad $H\gamma$ $\lambda 4340$, $H\beta$ $\lambda 4861$, and He I $\lambda 5876$ emission lines for the first time, which almost show same kinematic signatures. Specifically, the high-velocity gas in the wings exhibits a shorter lag than the low-velocity gas. However, the lag in the red wing is slightly larger than the lag in the blue wing, and the largest lag occurs in the red side. These complicated signatures should suggest that the BLR of Keplerian motion in Mrk 79 probably exists the outflow gas motion during the monitoring period.
5. Based on the velocity width and time delay of broad $H\beta$ $\lambda 4861$ line, we measured BH mass of $M_{\bullet} = 5.13_{-1.55}^{+1.57} \times 10^7 M_{\odot}$ for Mrk 79. This value is consistent with the estimate of $M_{\bullet} - \sigma_{*}$ relation. Using this BH mass and optical luminosity at 5100 \AA $L_{5100} =$

$(1.45 \pm 0.14) \times 10^{43} \text{ erg s}^{-1}$, we estimated accretion rates of $\dot{M}_\bullet = (0.05 \pm 0.02) L_{\text{Edd}} c^{-2}$. Mrk 79 is a sub-Eddington accreting AGN.

6. We found that the current $R_{\text{BLR}} - L_{5100}$ relation of Mrk 79 reverberation deviates from the canonical $R_{\text{BLR}} - L_{5100}$ (slope=0.53) and NGC 5548's $R_{\text{BLR}} - L_{5100}$ (slope=0.86) relationships. More and dense RM campaigns are necessary to construct robust $R_{\text{BLR}} - L_{5100}$ relationship of Mrk 79.

As discussed in Section 4, although we don't know whether blueshifted UV absorbers/emitters exist in Mrk 79 in absence UV spectrum, many findings including UFOs, warm absorbers, and the BLR kinematics of the high- and low-ionization gas, indicate that the BLR of Mrk 79 probably originates from disk wind launched from accretion disk. Nevertheless, simultaneous observations of multi-band spectra are necessary to confirm this speculation.

We are grateful to the referee for useful suggestions that improved the manuscript. We acknowledge the support of the staff of the Lijiang 2.4-m telescope. Funding for the telescope has been provided by CAS and the People's Government of Yunnan Province. This research is supported in part by National Key Program for Science and Technology Research and Development of China (grants 2016YFA0400701 and 2016YFA0400702). L.C.H. acknowledges financial support from the National Natural Science Foundation of China (NSFC; 11721303). K.X.L. acknowledges financial support from the NSFC (11703077) and from the Light of West China Program provided by CAS (No. Y7XB016001). MK was supported by the National Research Foundation of Korea (NRF) grant funded by the Korea government (MSIT) (No. 2017R1C1B2002879). W.H.B. acknowledges financial support from the NSFC (11973029).

REFERENCES

- Bahcall, J. N., Kozlovsky, B.-Z., & Salpeter, E. E. 1972, *ApJ*, 171, 467
 Baldwin, J., Ferland, G., Korista, K., et al. 1995, *ApJL*, 455, L119
 Barth, A. J., Bennert, V. N., Canalizo, G., et al. 2015, *ApJS*, 217, 26
 Barth, A. J., & Bentz, M. C. 2016, *MNRAS*, 458, L109
 Barth, A. J., Nguyen, M. L., Malkan, M. A., et al. 2011a, *ApJ*, 732, 121
 Barth, A. J., Pancoast, A., Bennert, V. N., et al. 2013, *ApJ*, 769, 128
 Barth, A. J., Pancoast, A., Thorman, S. J., et al. 2011b, *ApJL*, 743, L4
 Baskin, A., & Laor, A. 2018, *MNRAS*, 474, 1970
 Bentz, M. C., Denney, K. D., Cackett, E. M., et al. 2007, *ApJ*, 662, 205
 Bentz, M. C., Denney, K. D., Grier, C. J., et al. 2013, *ApJ*, 767, 149
 Bentz, M. C., Horne, K., Barth, A. J., et al. 2010, *ApJL*, 720, L46
 Bentz, M. C., Peterson, B. M., Netzer, H., Pogge, R. W., & Vestergaard, M. 2009a, *ApJ*, 697, 160
 Bentz, M. C., Walsh, J. L., Barth, A. J., et al. 2009b, *ApJ*, 705, 199
 Bian, W.-H., Huang, K., Hu, C., et al. 2010, *ApJ*, 718, 460
 Blandford, R. D., & McKee, C. F. 1982, *ApJ*, 255, 419
 Boroson, T. A., & Green, R. F. 1992, *ApJS*, 80, 109
 Bruzual, G., & Charlot, S. 2003, *MNRAS*, 344, 1000
 Collin-Souffrin, S. 1987, *A&A*, 179, 60
 Collin-Souffrin, S., & Dumont, A. M. 1990, *A&A*, 229, 292
 Czerny, B., & Hryniewicz, K. 2011, *A&A*, 525, L8
 Czerny, B., Li, Y.-R., Hryniewicz, K., et al. 2017, *ApJ*, 846, 154
 Denney, K. D., Peterson, B. M., Pogge, R. W., et al. 2010, *ApJ*, 721, 715
 Denney, K. D., Peterson, B. M., Pogge, R. W., et al. 2009a, *ApJL*, 704, L80
 Denney, K. D., Watson, L. C., Peterson, B. M., et al. 2009b, *ApJ*, 702, 1353
 Dehghanian, M., Ferland, G. J., Kriss, G. A., et al. 2019, *ApJ*, 877, 119
 De Rosa, G., Fausnaugh, M. M., Grier, C. J., et al. 2018, *ApJ*, 866, 133
 Dong, X.-B., Wang, J.-G., Ho, L. C., et al. 2011, *ApJ*, 736, 86
 Dong, X., Wang, T., Wang, J., et al. 2008, *MNRAS*, 383, 581
 Du, P., Hu, C., Lu, K.-X., et al. 2014, *ApJ*, 782, 45
 Du, P., Hu, C., Lu, K.-X., et al. 2015, *ApJ*, 806, 22
 Du, P., Lu, K.-X., Hu, C., et al. 2016, *ApJ*, 820, 27
 Du, P., Zhang, Z.-X., Wang, K., et al. 2018, *ApJ*, 856, 6
 Edelson, R., Turner, T. J., Pounds, K., et al. 2002, *ApJ*, 568, 610
 Fan, Y.-F., Bai, J.-M., Zhang, J.-J., et al. 2015, *Research in Astronomy and Astrophysics*, 15, 918
 Fausnaugh, M. M. 2017, *PASP*, 129, 024007
 Filippenko, A. 1982, *PASP*, 94, 715
 Gallo, L. C., Miniutti, G., Miller, J. M., et al. 2011, *MNRAS*, 411, 607
 Gaskell, C. M., & Peterson, B. M. 1987, *ApJS*, 65, 1
 Gaskell, C. M., & Sparke, L. S. 1986, *ApJ*, 305, 175
 Ge, X., Zhao, B.-X., Bian, W.-H., & Frederick, G. R. 2019, *AJ*, 157, 148
 Giustini, M., & Proga, D. 2019, arXiv:1904.07341
 Graham, A. W., Onken, C. A., Athanassoula, E., et al. 2011, *MNRAS*, 412, 2211
 Grier, C. J., Peterson, B. M., Horne, K., et al. 2013, *ApJ*, 764, 47
 Grier, C. J., Peterson, B. M., Pogge, R. W., et al. 2012, *ApJ*, 755, 60
 Grier, C. J., Trump, J. R., Shen, Y., et al. 2017, *ApJ*, 851, 21
 Hamann, F., Chartas, G., Reeves, J., & Nardini, E. 2018, *MNRAS*, 476, 943
 Ho, L. C. 2009, *ApJ*, 699, 638
 Ho, L. C., & Kim, M. 2014, *ApJ*, 789, 17
 Hu, C., Du, P., Lu, K.-X., et al. 2015, *ApJ*, 804, 138
 Hu, C., Wang, J.-M., Ho, L. C., et al. 2008, *ApJ*, 687, 78
 Hu, C., Wang, J.-M., Ho, L. C., et al. 2016, *ApJ*, 832, 197
 Jin, C., Ward, M., Done, C., & Gelbord, J. 2012, *MNRAS*, 420, 1825
 Kaspi, S., Smith, P. S., Netzer, H., et al. 2000, *ApJ*, 533, 631
 Kim, M., Ho, L. C., Peng, C. Y., Barth, A. J., & Im, M. 2008, *ApJS*, 179, 283
 Kim, M., Ho, L. C., Peng, C. Y., Barth, A. J., & Im, M. 2017, *ApJS*, 232, 21
 Kormendy, J., & Ho, L. C. 2013, *ARA&A*, 51, 511
 Kriss, G. A., De Rosa, G., Ely, J., et al. 2019, *ApJ*, 881, 153
 Leighly, K. M., & Moore, J. R. 2004, *ApJ*, 611, 107
 Liu, H.-Y., Yuan, W., Dong, X.-B., Zhou, H., & Liu, W.-J. 2018, *ApJS*, 235, 40
 Longinotti, A. L., Kriss, G., Krongold, Y., et al. 2019, arXiv:1903.05795
 Lu, K.-X., Du, P., Hu, C., et al. 2016, *ApJ*, 827, 118
 Lu, K.-X., Zhao, Y., Bai, J.-M., & Fan, X.-L. 2019, *MNRAS*, 483, 1722
 Maoz, D., Netzer, H., Leibowitz, E., et al. 1990, *ApJ*, 351, 75
 Markowitz, A., Reeves, J. N., George, I. M., et al. 2009, *ApJ*, 691, 922
 Mas-Ribas, L. 2019, arXiv:1903.08170
 Mehdipour, M., Kaastra, J. S., Kriss, G. A., et al. 2016, *A&A*, 588, A139
 Murray, N., & Chiang, J. 1997, *ApJ*, 474, 91
 Murray, N., Chiang, J., Grossman, S. A., & Voit, G. M. 1995, *ApJ*, 451, 498
 Nelson, C. H., Green, R. F., Bower, G., Gebhardt, K., & Weistrop, D. 2004, *ApJ*, 615, 652
 O'Brien, P. T., Reeves, J. N., Simpson, C., & Ward, M. J. 2005, *MNRAS*, 360, L25
 Parker, M. L., Buisson, D. J. K., Jiang, J., et al. 2018, *MNRAS*, 479, L45
 Pei, L., Fausnaugh, M. M., Barth, A. J., et al. 2017, *ApJ*, 837, 131
 Peng, C. Y., Ho, L. C., Impey, C. D., & Rix, H.-W. 2002, *AJ*, 124, 266
 Peterson, B. 1993, *PASP*, 105, 247
 Peterson, B. M. 2014, *SSRv*, 183, 253
 Peterson, B. M., Ali, B., Horne, K., et al. 1993, *ApJ*, 402, 469
 Peterson, B. M., Barth, A. J., Berlind, P., et al. 1999, *ApJ*, 510, 659

Peterson, B. M., Berlind, P., Bertram, R., et al. 2002, *ApJ*, 581, 197
 Peterson, B. M., Ferrarese, L., Gilbert, K. M., et al. 2004, *ApJ*, 613, 682
 Peterson, B. M., Pogge, R. W., Wanders, I., et al. 1995, *PASP*, 107, 579
 Peterson, B. M., Wanders, I., Horne, K., et al. 1998, *PASP*, 110, 660
 Planck Collaboration, Ade, P. A. R., Aghanim, N., et al. 2014, *A&A*, 571, A16
 Richards, G. T., Kruczek, N. E., Gallagher, S. C., et al. 2011, *AJ*, 141, 167
 Rodríguez-Pascual, P. M., Alloin, D., Clavel, J., et al. 1997, *ApJS*, 110, 9
 Schlegel, D. J., Finkbeiner, D. P., & Davis, M. 1998, *ApJ*, 500, 525
 Schmitt, H. R., Donley, J. L., Antonucci, R. R. J., et al. 2003a, *ApJS*, 148, 327
 Schmitt, H. R., Donley, J. L., Antonucci, R. R. J., et al. 2003b, *ApJ*, 597, 768
 Stern, J., & Laor, A. 2012, *MNRAS*, 423, 600
 Tombesi, F., Cappi, M., Reeves, J. N., et al. 2010, *A&A*, 521, A57

APPENDIX

A. INSIGHT INTO THE SPECTROSCOPY AND CALIBRATION

To qualitatively study the apparent variation in flux of the host galaxy and the [O III] $\lambda 5007$ mentioned in Section 3.1 and 3.4, we have insight into the details of spectroscopy and flux calibration in this Appendix. Mrk 79 consist of the AGN (including the BLR), the host galaxy and the [O III] emission region (i.e., NLR: the narrow-line region), which is observed along with the comparison star simultaneously. At first, we simply considered the size of different components. The AGN including the BLR along with the comparison star are point sources, the intrinsic size of point source approximates $0''$ in remote distance. For the NLR and the host galaxy, we noted that Peterson et al. (1995) have produced the models of the surface-brightness distribution of the NLR and host-galaxy distribution from ground-based images in NGC 4151 and NGC 5548, and found that (1) the NLR of NGC 5548 is point-like source; (2) The NLR of NGC 4151 is slightly extended source. Based on the growth curve for the [O III] $\lambda 5007$ flux distribution constructed by Peterson et al. (1995), we estimated the radius (defined by 80% of the integrated [O III] $\lambda 5007$ flux) of the [O III] emission region in NGC 4151 ($\sim 1.5''$); (3) The host galaxy is very extended source, this is consistent with the results of *HST* image decomposition for the local AGNs (see Bentz et al. 2009a; Kim et al. 2017). In Mrk 79, based on *HST* image of the [O III], Schmitt et al. (2003a) measured the effective radius (defined by 50% of the integrated [O III] $\lambda 5007$ flux), extent of photometric semi-major and semi-minor axes of the [O III] emission (see Table 3 of Schmitt et al. 2003a). The semi-major axes, which is roughly perpendicular to our long slit (see Figure 8 of Schmitt et al. 2003a, and the position angle of our long slit is -99°), has a size of $2.1''$, comparable to the width of slit. This valuable measurement shows the NLR of Mrk 79 along with a part of other AGNs is slightly extended source. For AGNs with a slightly extended NLR observed with a broad spectrograph slit of $5.0''$ (adopted by many previous RM campaigns, see Table 12 of Bentz et al. 2013), standard spectral calibration method using the [O III] $\lambda 5007$ as calibrator provides precise internal flux calibration of spectra (see Fausnaugh 2017; Peterson et al. 1995), because broad spectrograph slit integrally observed

Tombesi, F., Cappi, M., Reeves, J. N., et al. 2011, *ApJ*, 742, 44
 Tombesi, F., Cappi, M., Reeves, J. N., et al. 2013, *MNRAS*, 430, 1102
 Ulrich, M.-H., Boksenberg, A., Bromage, G. E., et al. 1991, *ApJ*, 382, 483
 Wandel, A., Peterson, B. M., & Malkan, M. A. 1999, *ApJ*, 526, 579
 Wang, C.-J., Bai, J.-M., Fan, Y.-F., et al. 2019, arXiv:1905.05915
 Wang, J.-G., Dong, X.-B., Wang, T.-G., et al. 2009, *ApJ*, 707, 1334
 Wang, J.-M., Du, P., Brotherton, M. S., et al. 2017, *Nature Astronomy*, 1, 775
 Whittle, M. 1992, *ApJS*, 79, 49
 White, R. J., & Peterson, B. M. 1994, *PASP*, 106, 879
 Xiao, M., Du, P., Lu, K.-K., et al. 2018, *ApJL*, 865, L8
 Zhang, Z.-X., Du, P., Smith, P. S., et al. 2019, *ApJ*, 876, 49
 Zu, Y., Kochanek, C. S., & Peterson, B. M. 2011, *ApJ*, 735, 80

[O III] $\lambda 5007$ emission of AGNs. This is not the case for a small spectrograph slit ($2.5''$), the seeing-induced aperture effects will cause the apparent variation in flux of extended source. We give a quantitative analysis about this point in the next, in fact, which is similar to Peterson et al. (1995)'s analysis of aperture effects on the accuracy of ground-based spectrophotometry.

Figure A1 is a spectroscopic schematic diagram for showing the flux variation of different components in the slit. We use red and blue Gaussian profiles to present the surface-brightness distribution of these components broadened by different seeing (in practice, the slightly or very extended source has a flatter surface-brightness distribution than Gaussian profile, see Peterson et al. 1995). For each component, the area surrounded by red and blue Gaussians within the small slit present the fractions of light loss caused by varying seeing. Figure A1 shows that the fractions of light loss due to varying observing conditions (e.g., seeing) are dependent on the size of the object (i.e., the width of surface-brightness distribution), seeing and the width of slit (also see Peterson et al. 1995). If we use ψ^{star} , ψ^{AGN} , $\psi^{\text{[O III]}}$, and ψ^{gal} to represent the percentage of flux remaining in the aperture for different components, the observed flux can be described by

$$F_{\text{obs}}^{\text{star}} = \psi^{\text{star}} \times F_{\text{abs}}^{\text{star}} \quad (\text{A1})$$

for the comparison star,

$$F_{\text{obs}}^{\text{AGN}} = \psi^{\text{AGN}} \times F_{\text{abs}}^{\text{AGN}} \quad (\text{A2})$$

for the AGN,

$$F_{\text{obs}}^{\text{[O III]}} = \psi^{\text{[O III]}} \times F_{\text{abs}}^{\text{[O III]}} \quad (\text{A3})$$

for [O III] $\lambda 5007$ (from the extended NLR), and

$$F_{\text{obs}}^{\text{gal}} = \psi^{\text{gal}} \times F_{\text{abs}}^{\text{gal}} \quad (\text{A4})$$

for the host galaxy, where F_{abs} are the absolute fluxes of these components.

The observed flux F_{obs} is corrected by multiplying to the flux-calibration factor, the factor is obtained by comparing the absolute flux to the observed flux of the comparison star (Maoz et al. 1990; Kaspi et al. 2000; Du et al. 2014), that is the calibrated flux

$$F_{\text{cal}} = F_{\text{obs}} \times \frac{F_{\text{abs}}^{\text{star}}}{F_{\text{obs}}^{\text{star}}} = \frac{1}{\psi^{\text{star}}} \times F_{\text{obs}}. \quad (\text{A5})$$

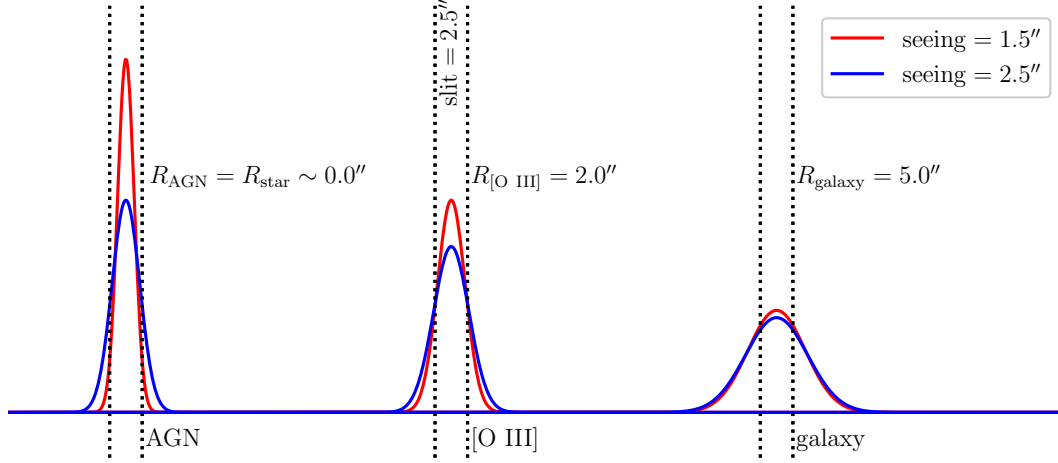


Figure A1. Schematic diagram for showing the flux variation in the slit. Each pair of dotted lines represent the slit (width= $2.5''$) adopted in spectroscopy. The Gaussian profiles (left to right) represent the flux distribution (i.e., surface-brightness distribution) of the point sources (AGN, the BLR and star), the slightly extended source ([O III]) and the very extended source (host galaxy), respectively. The red profiles are broadened by seeing of $1.5''$, the blue profiles are broadened by seeing of $2.5''$. R_{star} , R_{AGN} , $R_{\text{[O III]}}$ and R_{galaxy} roughly represent the radii of the comparison star, AGN, [O III] emission region (refer to Schmitt et al. 2003a) and the host galaxy (refer to Bentz et al. 2009a), respectively.

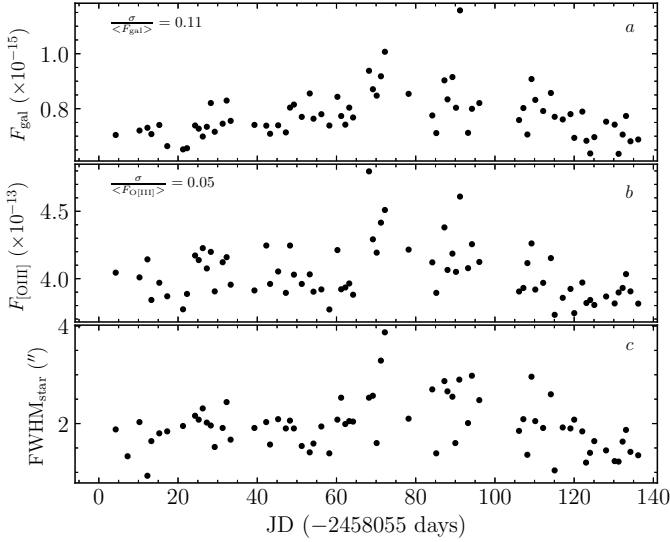


Figure A2. Panels (a-b) are the apparent variation in fluxes of the host galaxy and [O III] $\lambda 5007$ measured from the best-fit components. The width (FWHM_{star}) of star's flux distribution was measured from the short exposure image, the image was observed before and near the spectroscopy. Panel (c) shows the variation of FWHM_{star}.

Therefore, we deduced the calibrated flux of the AGN

$$\begin{aligned} F_{\text{cal}}^{\text{AGN}} &= \frac{1}{\psi_{\text{star}}} \times F_{\text{obs}}^{\text{AGN}} \\ &= \frac{\psi^{\text{AGN}}}{\psi_{\text{star}}} \times F_{\text{abs}}^{\text{AGN}} = f_{\text{cal}}^{\text{AGN}} \times F_{\text{abs}}^{\text{AGN}}, \end{aligned} \quad (\text{A6})$$

the extended NLR

$$\begin{aligned} F_{\text{cal}}^{[\text{O III}]}} &= \frac{1}{\psi_{\text{star}}} \times F_{\text{obs}}^{[\text{O III}]}} \\ &= \frac{\psi^{[\text{O III}]}}{\psi_{\text{star}}} \times F_{\text{abs}}^{[\text{O III}]}} = f_{\text{cal}}^{[\text{O III}]}} \times F_{\text{abs}}^{[\text{O III}]}} \end{aligned} \quad (\text{A7})$$

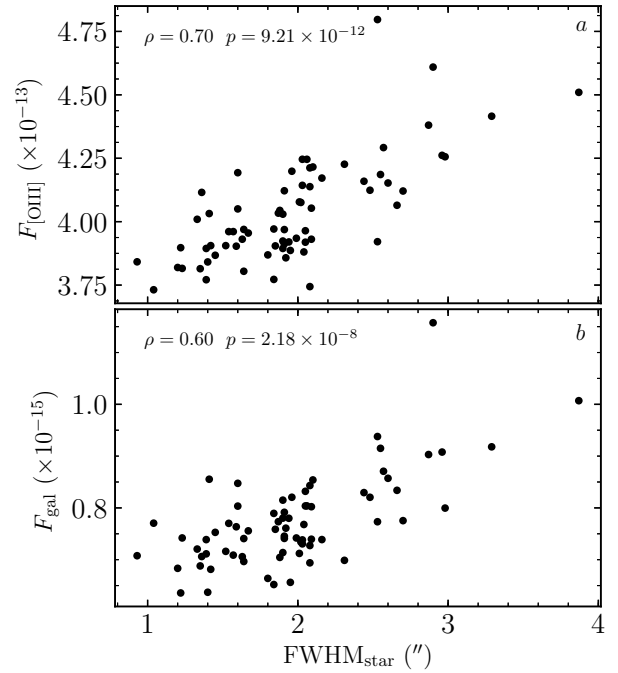


Figure A3. Relation between the fluxes of extended components ($F_{\text{[O III]}}$ and F_{gal}) and FWHM_{star} variation. Spearman rank-order correlation coefficient (ρ) and the p-value (p) are noted in the panels.

and the host galaxy

$$\begin{aligned} F_{\text{cal}}^{\text{gal}} &= \frac{1}{\psi_{\text{star}}} \times F_{\text{obs}}^{\text{gal}} \\ &= \frac{\psi^{\text{gal}}}{\psi_{\text{star}}} \times F_{\text{abs}}^{\text{gal}} = f_{\text{cal}}^{\text{gal}} \times F_{\text{abs}}^{\text{gal}}. \end{aligned} \quad (\text{A8})$$

Where f_{cal} are the flux-calibration factors of different components.

Figure A1 also shows that two point sources (the comparison star and AGN) kept in a line parallel to the slit, the frac-

tions of light loss due to varying seeing are identical. However, the extended component (the [O III] emission region and the host galaxy) in the same slit, the fractions of light loss due to varying seeing are less than point source (similar analysis about aperture effects are addressed in Section 2.1 of Peterson et al. 1995). In this case, for Mrk 79, the radii of different components including the AGN, the NLR, and the host galaxy meet $R_{\text{AGN}}(\sim 0'') < R_{\text{NLR}}(\sim 2'') < R_{\text{gal}}(\sim 5'')$ relation. When seeing increases, the percentages of flux remaining in the aperture meet $\psi^{\text{AGN}} = \psi^{\text{star}} < \psi^{[\text{O III}]} < \psi^{\text{gal}}$ relation. The result is that the flux-calibration factors meet $1 = f_{\text{cal}}^{\text{AGN}} < f_{\text{cal}}^{[\text{O III}]} < f_{\text{cal}}^{\text{gal}}$ relation. That is the most extended component has the largest flux calibration factor. Consequently, (1) the flux-calibration factor of extended component should correlate with seeing, that is the calibrated fluxes including $F_{\text{cal}}^{[\text{O III}]}$ and $F_{\text{cal}}^{\text{gal}}$ (Equation A7 and A8) should correlate with seeing because the absolute flux (including $F_{\text{abs}}^{[\text{O III}]}$ and $F_{\text{abs}}^{\text{gal}}$) is constant; (2) the host-galaxy fluxes ($F_{\text{cal}}^{\text{gal}}$) should be more scatter than [O III]'s fluxes ($F_{\text{cal}}^{[\text{O III}]}$) since $f_{\text{cal}}^{\text{gal}}$ is larger than $f_{\text{cal}}^{[\text{O III}]}$ with varying seeing.

In order to test the above analysis results from the perspective of observation, we measured the width ($\text{FWHM}_{\text{star}}$) of

the star's flux distribution from the short exposure image observed before and near the spectroscopy, and showed the variation of $\text{FWHM}_{\text{star}}$ in Figure A2 (panel c). In practice, seeing could change from one exposure to the next, $\text{FWHM}_{\text{star}}$ is mainly modulated by varying seeing. Figure A2 shows that the apparent variations in fluxes of the extended components (including [O III] emission region and the host galaxy) are similar to the variation of $\text{FWHM}_{\text{star}}$, and the host-galaxy fluxes (11%) are more scatter than [O III]'s fluxes (5%). Figure A3 clearly shows that the fluxes of extended components correlate with the variation of $\text{FWHM}_{\text{star}}$. Actually, these examination results are consistent with above analysis, and show that the [O III] emission region in Mrk 79 is slightly extended source. Therefore, for a narrow slit, the varying observing conditions will give rise to the apparent variation in flux of the extended components. So that the [O III] remains in the rms spectrum and its fluxes have a scatter of 5%.

B. VELOCITY-RESOLVED REVERBERATION MAPPING

In Section 3.8, we presented the procedure of velocity-resolved reverberation mapping. In this appendix, we provide the velocity-dependent light curves and cross correlation analysis including $\text{H}\beta$ $\lambda 4861$, $\text{H}\gamma$ $\lambda 4340$, He II $\lambda 4686$ and He I $\lambda 5876$ (see Figures B4, B5, B6, B7)

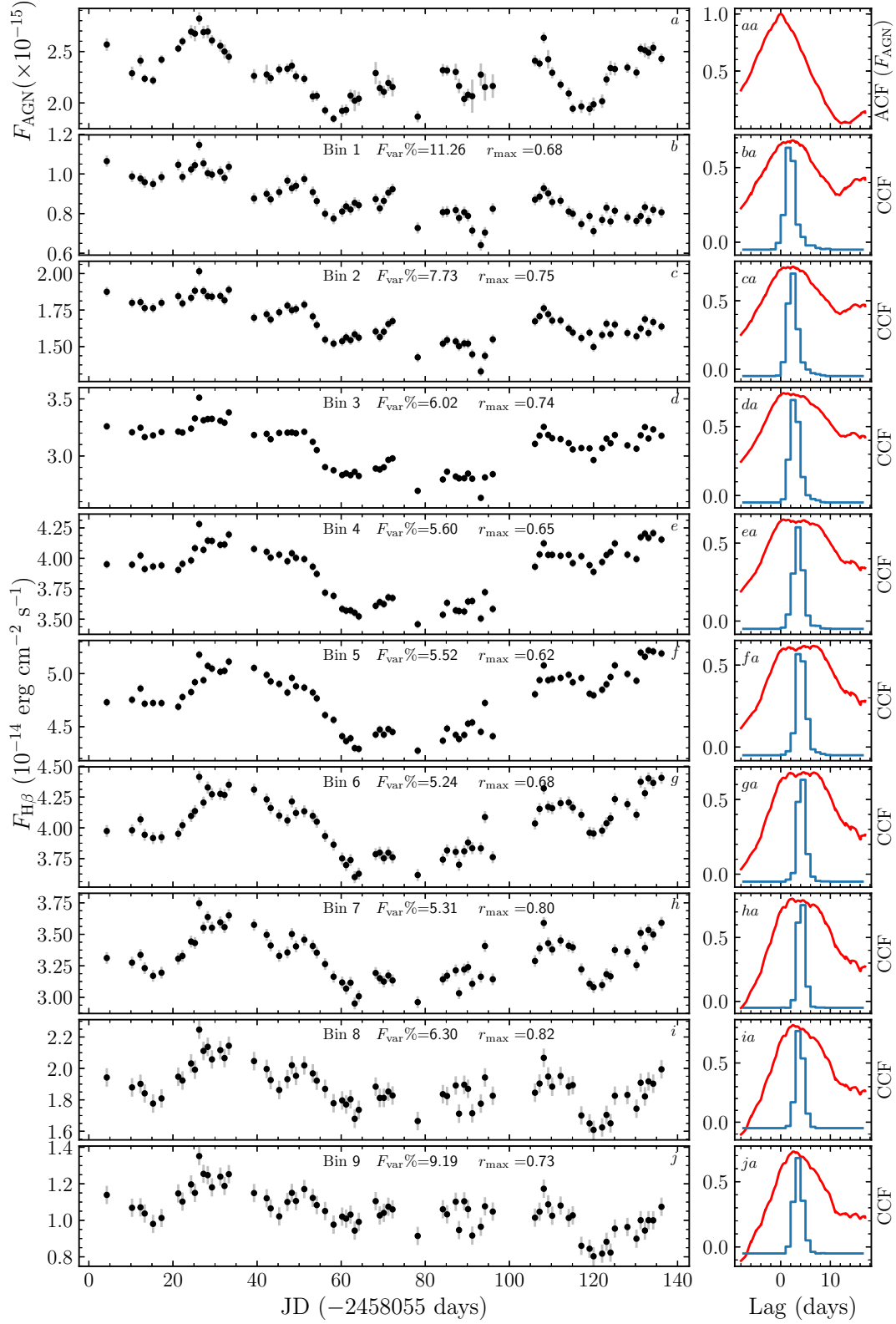


Figure B4. Velocity-resolved reverberation mapping. The left panels (*a-j*) show the light curves of AGN continuum at 5100 Å and the broad H β emission line of each velocity bin, respectively. We noted the variability amplitude of the light curves in panels (*b-j*). The right panels (*aa-ja*) correspond to the ACF of continuum at 5100 Å and the CCF between the light curve of each velocity bin (*b-j*) and the continuum variation (*a*), respectively. We noted the maximum correlation coefficients (r_{max}) in panels (*b-j*). Monte Carlo simulations of the centroid (blue) are over-plotted in panels (*ba-ja*). Bin number (Bin 1–9) is one-to-one correspondence with Figure 7.

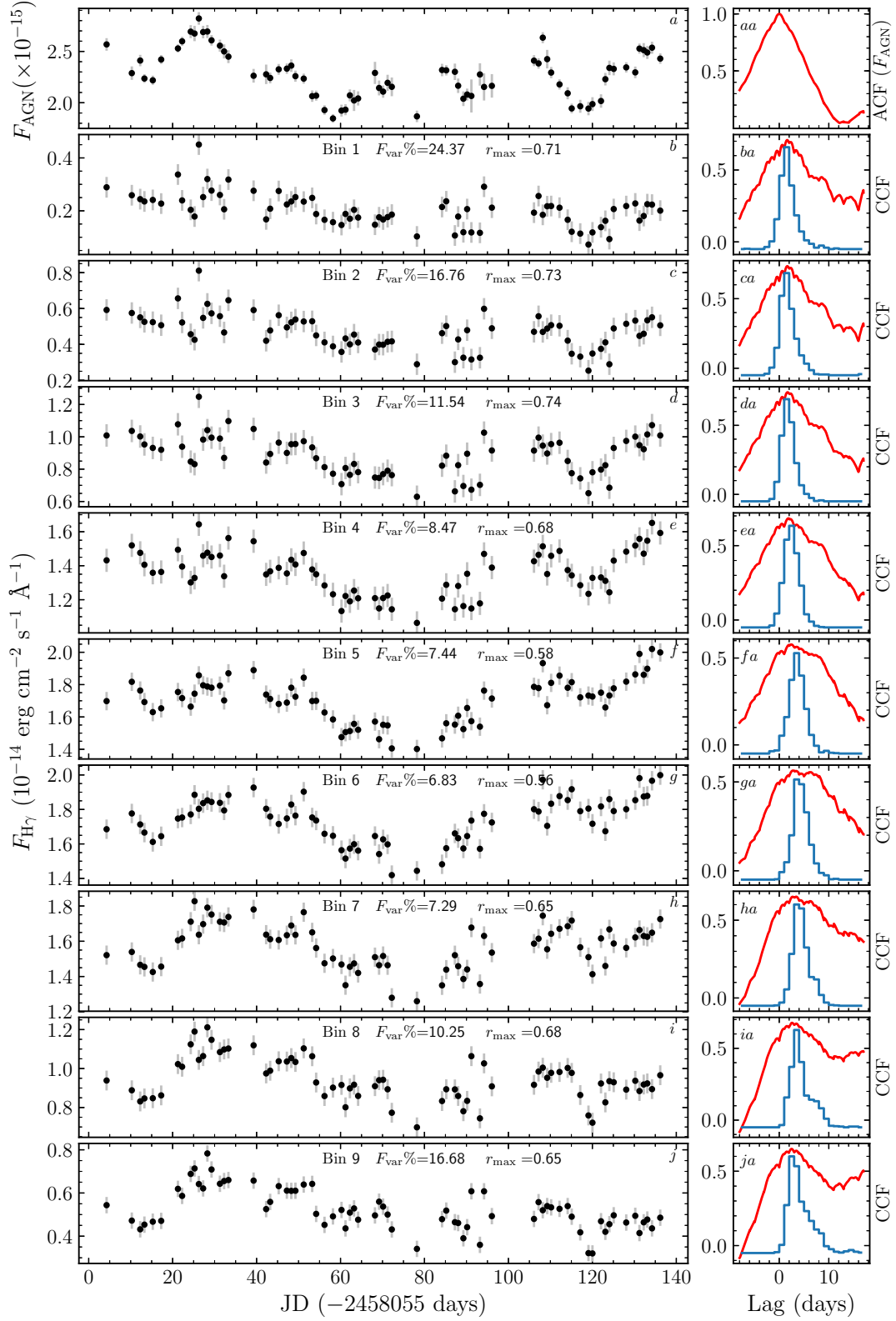


Figure B5. Same as Figure B4, but for the broad H γ emission line.

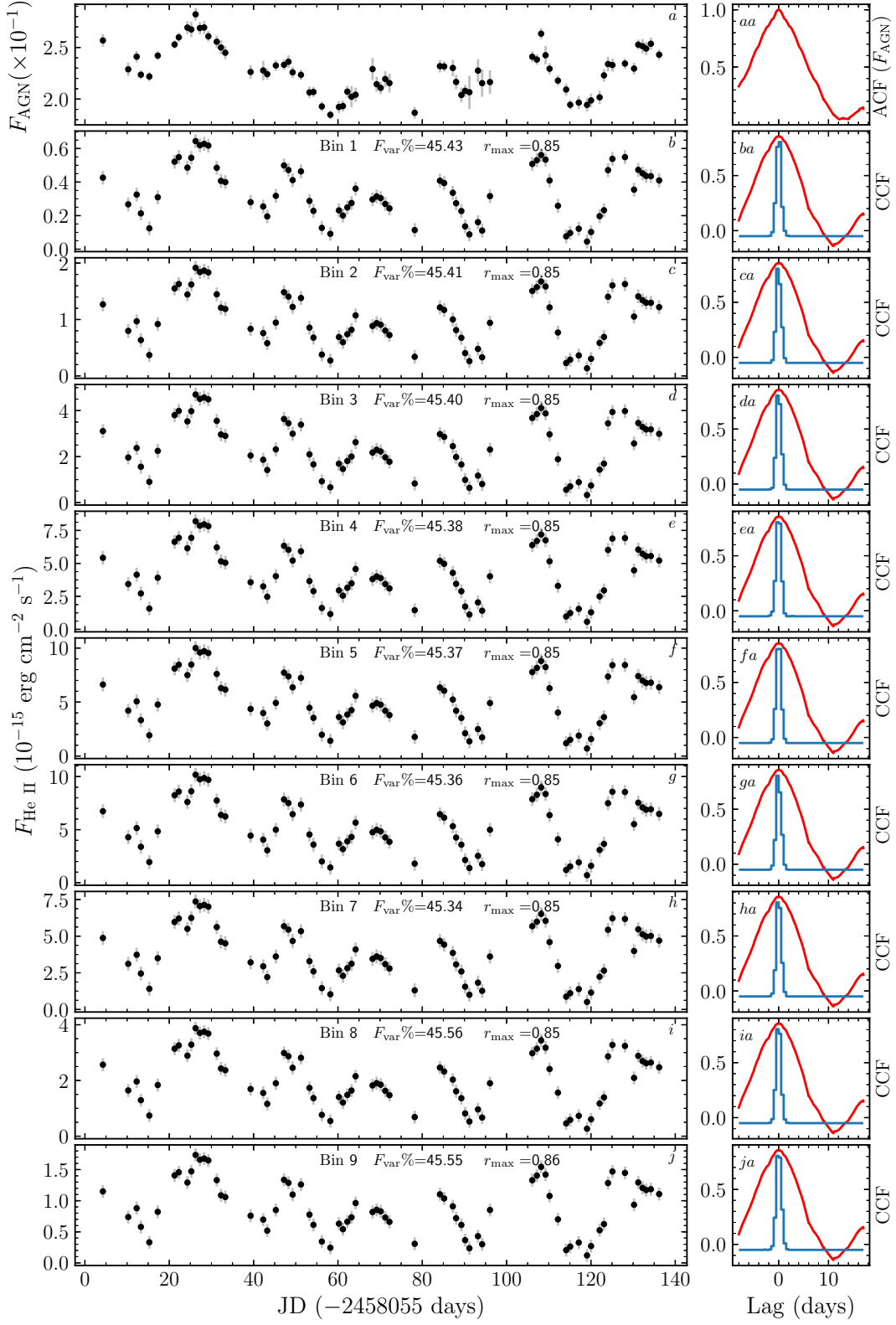


Figure B6. Same as Figure B4, but for the broad He II emission line.

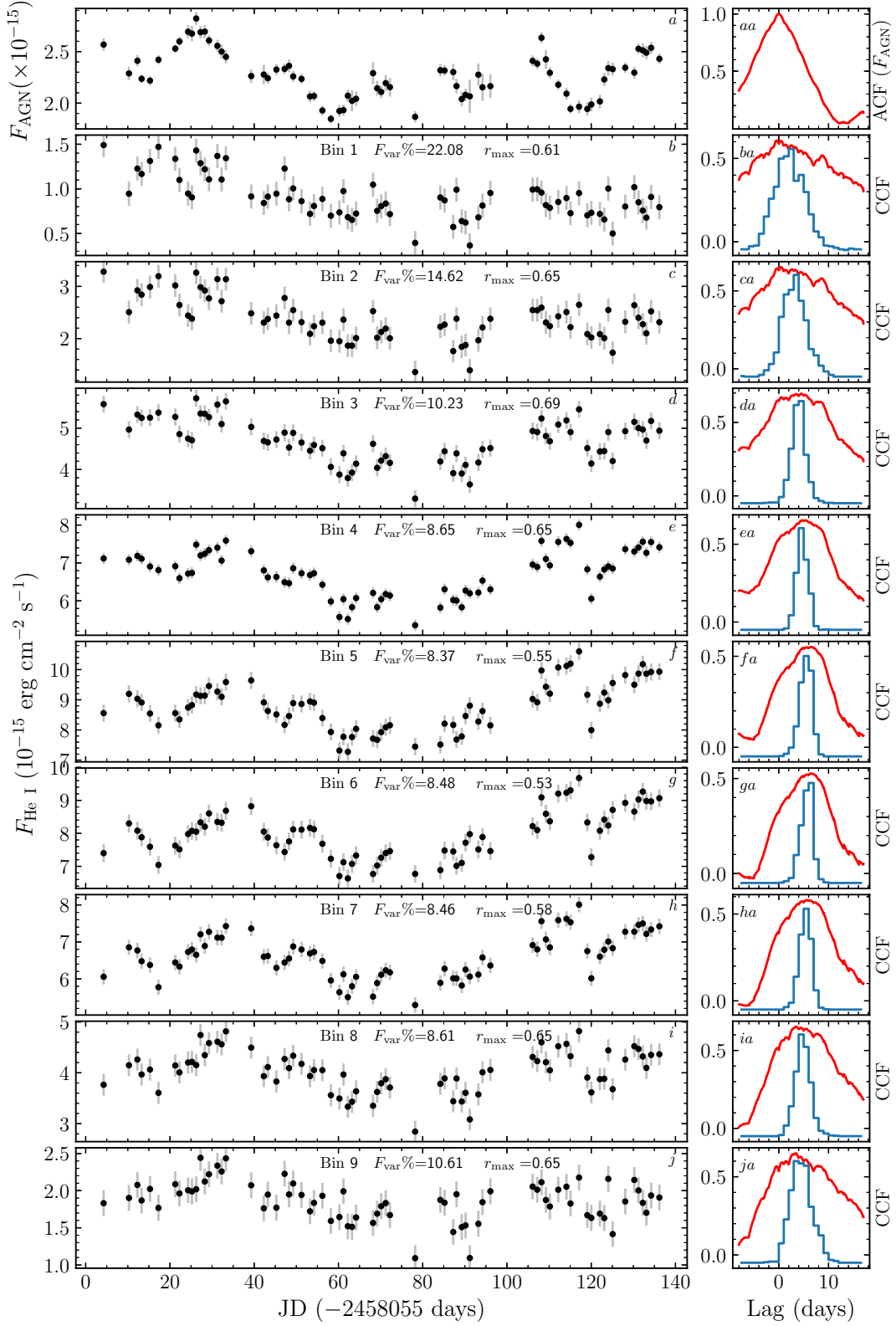


Figure B7. Same as Figure B4, but for the broad He I emission line.